Journal of the Mechanics and Physics of Solids 125 (2019) 178–197

Contents lists available at ScienceDirect

Journal of the Mechanics and Physics of Solids

journal homepage: www.elsevier.com/locate/jmps

Biomimetic architected materials with improved dynamic performance

Zian Jia[a], Yang Yu[a,b], Shaoyu Hou[a], Lifeng Wang[a,*]

[a] *Department of Mechanical Engineering, State University of New York at Stony Brook, Stony Brook, New York 11794, USA*
[b] *Department of Mechanics, School of Aerospace Engineering, Beijing Institute of Technology, Beijing 100081, China*

ARTICLE INFO

Article history:
Received 16 September 2018
Revised 17 December 2018
Accepted 20 December 2018
Available online 23 December 2018

Keywords:
Biomimetic
Architected material
Dynamic impact
Fracture control
Toughening mechanism

ABSTRACT

In recent decades, material performances improved by the discovery of new bulk materials have slowed down. By contrast, novel and unprecedented material properties have been demonstrated under the concept of “architected materials”, where the material properties are dominated by material microstructure instead of constituents. Knowing that mother nature is “a master of material architecture” through millions of years evolution – nearly all natural materials have elegantly fine and organized structures showing excellent impact resistance and damage tolerance. In this study, we design material architectures mimicking biomaterials and 3D print architected beams with dynamic performance far beyond their bulk constituents. By performing dynamic three-point bending tests and digital image correlation analysis, we characterize five types of bioinspired microstructures and propose the criteria of architecture selection adopting the concept of material indices. The reason why certain microstructures are preferred by certain organisms and how to optimally select material architectures for specific engineering applications are illustrated. Furthermore, microstructure integration approaches that work on multiple length scales (hierarchical designs) and on one specific length scale (hybrid designs) are investigated. Applying these approaches, we have designed architected beams that are flexible and strong, strong and tough, dissipative and stiff, and flexible and responsive, which are typically exclusive in bulk materials. Additionally, material architectures give extra control of fracture patterns, improving the critical impact energy by over 6 times. This work provides insights to the structure–property relationships and will facilitate the development of architected materials with tailored performances of flexibility, strength, toughness, energy dissipation, and fast response.

1. Introduction

The progress of engineering materials has long been depending on the material constituents – from bronze and iron in the ancient, to polymers, super alloys, and graphene in the modern time (Ashby and Johnson, 2013). In recent decades, the discovery of new bulk materials has slowed down, by contrast, the study of architected materials has increased exponentially, offering a new approach to obtain unprecedented material properties (Bechthold and Weaver, 2017; Montemayor et al., 2015). Architected materials (also known as micro-architected materials or structured materials) refer to materials

---

[*] Corresponding author.
E-mail address: lifeng.wang@stonybrook.edu (L. Wang).

https://doi.org/10.1016/j.jmps.2018.12.015
0022-5096/© 2018 Elsevier Ltd. All rights reserved.

with finely designed microstructures, which potentially bring exceptional mechanical (Berger et al., 2017; Zheng et al., 2014), thermal (Chen et al., 2016; Maldovan, 2013), phononic (Gorishnyy et al., 2005; Jia et al., 2018a; Khelif et al., 2003), and other physical properties like negative material index (Coulais et al., 2017; Kadic et al., 2012; Klatt and Haberman, 2013; Nicolaou and Motter, 2012). Importantly, the properties of architected materials are dominated by the material microstructure instead of constituents, and the precise control of material distribution gives a more efficient use of the constituents, expanding the property space beyond that of bulk materials (Montemayor et al., 2015). For example, while metals are traditionally strengthened by alloying with impurity elements, recent researches find that introducing low-energy interfaces (e.g., nanotwin lamellae) and tailoring the distribution of these interfaces at the nanoscale produce metals that are stable, strong, ductile, and highly conductive (Lu, 2016; Lu et al., 2004). Recently, steels are 3D printed with hexagonal dislocation networks enabled by ultra-high cooling rate. These networks work as “soft” barriers that hinder dislocation motion but allow continuous plastic flow, creating an ideal combination of strength and ductility (Liu et al., 2018). Periodic foams with closed unit cells are demonstrated to reach the Hashin–Shtrikman upper bounds of stiffness for an isotropic material (Berger et al., 2017). Moreover, the fracture energy of ceramics has been improved by 2∼3 orders by staggering ceramic sheets in a “brick and mortar” architecture (Bouville et al., 2014; Clegg et al., 1990; Munch et al., 2008), solving the brittle problem of traditional ceramics. Other discussions on material architectures can be found in lattice materials (Chen and Wang, 2016; Meza et al., 2015; Schaedler et al., 2011), cellular materials (Schaedler and Carter, 2016; Wang et al., 2009a), and interpenetrating phase materials (Al-Ketan et al., 2017; Wang et al., 2011), for which references (Bechthold and Weaver, 2017; Bertoldi et al., 2017; Meyers et al., 2013; Montemayor et al., 2015; Velasco-Hogan et al., 2018; Wegst et al., 2015) give comprehensive reviews.

All these achievements show the promising future of architected materials. Despite our great advances in architected material design and fabrication, the synthetic architected materials still can’t match that of the natural materials (Meyers et al., 2013; Wegst et al., 2015). Through millions of years of evolution, nature is indeed “a master of material architecture” – nearly all natural materials have elegantly fine and organized structures possessing fantastic material properties. Interestingly, they are built from limited component materials with relatively poor properties but possess superior traits stemming from their complex architectures over multiple length scales (Studart, 2012; Wegst et al., 2015). Therefore, natural materials offer great inspirations for designing architected engineering materials. In fact, scientists have long been fascinated by natural materials for their light weight, high strength, toughness and multifunction, among which, woods, bones, teeth, sea shells, and bamboo has been extensively studied (Currey, 1999; Jackson et al., 1988; Launey et al., 2010; Mirkhalaf et al., 2014). Microstructures and hierarchy are two important features of biomaterials (Fratzl, 2007; Gao, 2006). Specifically, material microstructures achieve enhanced mechanical functions by using hard components to resist wear and provide stiffness, while using soft interfaces to accommodate deformations, which facilitate toughening mechanisms include microcracking, crack deflection, ligament bridging, fibril sliding, and molecular uncoiling (Launey et al., 2010; Ritchie, 2011). On the other hand, hierarchy spans multiple length scales and ensures that the microstructures at different length scales work synergistically (Gao, 2006; Lakes, 1993; Zhang et al., 2011). The complexity of microstructures, especially hierarchies spanning several length scales has long been challenging for artificial synthesis and experimental investigations.

Recently, additive manufacturing methods like 3D printing enable researchers to fabricate architected materials with intricate microstructures and have been widely used in studying the structure-property relationship (Dimas et al., 2013; Martin et al., 2017; Meza et al., 2015; Raney et al., 2018; Wang et al., 2011). For example, staggered microstructures inspired from bones (Dimas et al., 2013) have been printed with a multi-material printer, and 20 times increasement in fracture energy was obtained under static tensile loading. Cross-lamellar microstructures mimicking the conch shell improves fracture energy by 85% under drop tower tests (∼3 m/s) (Gu et al., 2017b). In addition, 3D printing also helps to unravel the toughening role of osteon shape (Libonati et al., 2016) and mineral bridges (Gu et al., 2017a) in biomaterials. More recently, metals with dislocations arranged in hexagonal networks are printed with selective laser melting methods, which show simultaneously high strength and ductility (Liu et al., 2018). Aside from toughness, it has been shown that the damping performance can be improved by over 100% with staggered microstructures (Zhang et al., 2015). Furthermore, with the aid of magnetic fields, discontinuous fibers arranged in concentric (Martin et al., 2015), layer (Compton and Lewis, 2014), and spiral patterns (Raney et al., 2018) (mimicking that of bone osteon, nacre, and stomatopod respectively) have been successfully printed, which offer great control over the stiffness. However, the improvement in strength is limited (40%) and the work of fracture decreases adversely (Raney et al., 2018), probably due to the relatively low fiber volume fraction and the defects induced during the printing process.

These works on printing biomimetic microstructures improve our understanding of the role of material architecture, yet more questions must be answered. First, most of the current researches of biomaterials focus on one specific material architecture and seldom are their disadvantages highlighted. The fact that organisms evolve various microstructures based on different requirements (different functions and loading conditions) suggests that different biostructures should have different specifications. As such, a systematic and fair comparison between different microstructures focusing on both their pros and cons are very helpful for realistic design of architected materials. Second, there are many parameters that can be used to characterize a material. Hence, an easy way of visualizing various material properties and how to use one comprehensive parameter in the comparison and selection of material architectures are of special interest. Here the concept of material indices (Ashby, 2016) will be adopted for this purpose. Third, most previous studies focus on the static performance and the improvement of dynamic performance achieved so far is not as significant (∼85%) (Gu et al., 2017b). Thereby, 3D printed architectures that further improve the impact protection ability are of great interest. Fourth, how to rationally inte-

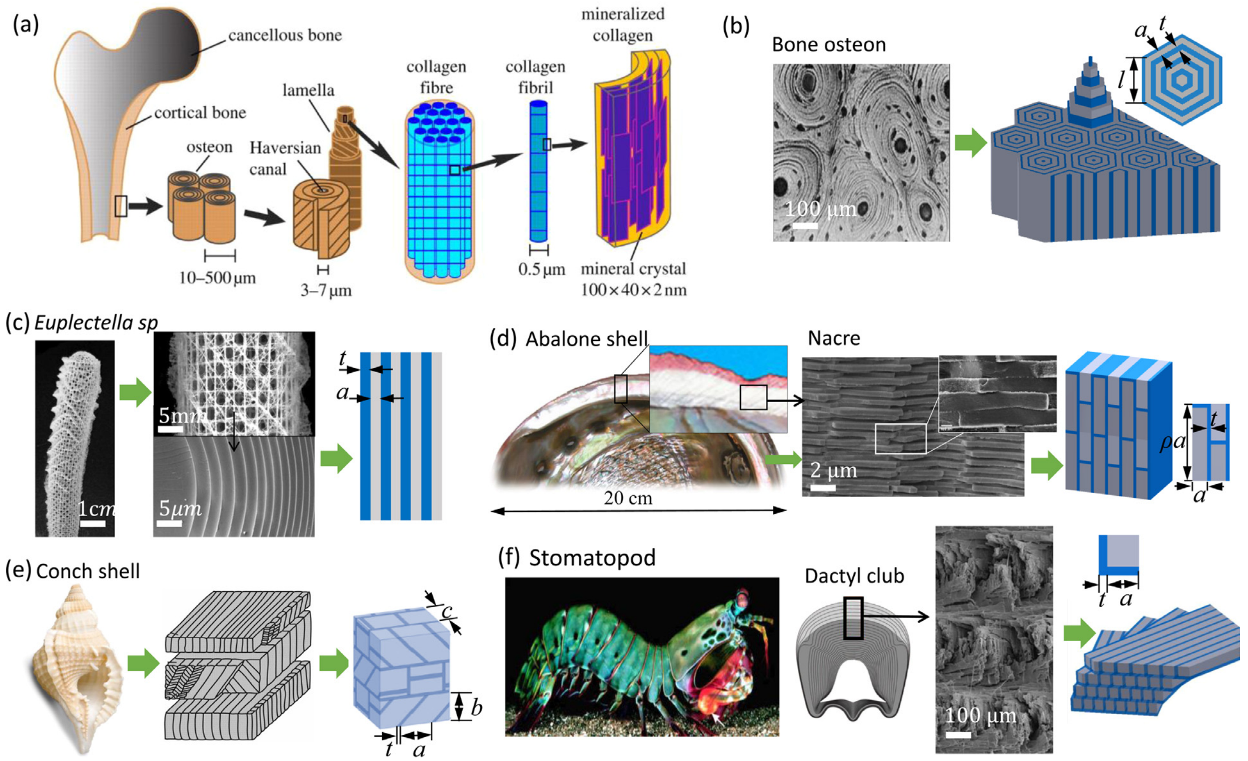

Fig. 1. Biomimetic microstructures. (a) The architecture of bone with five levels of hierarchy. Image is adopted from (Zhang et al., 2011). (b) SEM picture of bone osteon and corresponding concentric hexagonal unit cell modeling. (c-f) show the optical pictures, SEM pictures, and microstructures of sea sponge, nacre, conch shell, and stomatopod dactyl club, respectively. The grey and blue color in the schematics represent the hard phase and soft phase, respectively. Also marked are the geometric parameters used to define the unit cells. The SEM images in (b-f) are adopted from (Aizenberg et al., 2005; Barthelat et al., 2007; Weaver et al., 2012; Zhang et al., 2011), respectively. (For interpretation of the references to color in this figure legend, the reader is referred to the web version of this article.)

grate different microstructures, especially when the order of hierarchy is limited by the fabrication method remains largely unexplored. In addition, recent advances in topics like soft robotics and wearable devices pose new requirements like flexibility, short response time, and tunable dissipation. Therefore, a systematic research on the relationship between material architectures and dynamic properties is highly desired.

In this work, we first design and fabricate architected beams with layer, brick-and-mortar, concentric hexagonal, cross-lamellar, and rotating plywood microstructures using a multi-material 3D printer, mimicking sea sponge, nacre, bone osteon, conch shell, and stomatopod dactyl club, respectively. These specimens are tested with low-velocity three-point bending ($2\sim12$ m/s), from which material performances including energy dissipation, response time, flexibility, stiffness, strength, and toughness are evaluated. Based on the experimental data, the signature character of each microstructure is analyzed, and material indices are used for quantitative analysis. Furthermore, two microstructural integration approach are investigated, and theoretical analysis are adopted to analyze the mechanisms of toughening and fast response.

2. Materials and methods

2.1. Microstructure design and specimen fabrication

In this study, the architected materials are restrained to be composed of a hard phase and a compliant phase. Five basis microstructures are studied, i.e., the layer, brick and mortar, concentric hexagon, cross-lamellar, and rotating plywood microstructures (Fig. 1). Layered microstructures are ubiquitous in nature like sea sponges (Aizenberg et al., 2005) and articular cartilage (Zhao et al., 2011), which is an essential micro-component of other architectures like concentric ring and cross-lamellar. The brick and mortar structure is first reported by Jackson in nacre (Jackson et al., 1988), and its outstanding toughness has been demonstrated by many researchers (Barthelat et al., 2007; Dimas et al., 2013). It is one of the several distinct architectures found in bivalve shells. By contrast, cross-lamellar structure (Menig et al., 2001; Shin et al., 2016) is the most common throughout the phylum, occurring in the Classes *Bivalvia, Gastropoda, Polyplacophora* and *Scaphopoda* (Currey and Kohn, 1976). Here, the cross-lamellar model is adopted from (Gu et al., 2017b) for comparison. Moreover, the concentric structures are found in bone osteons, tree annual rings, and bamboos, which protect the vessels inside.

Table 1
Performance of beams made with consitituent bulk materials.

Material	VeroWhite	Tango Plus
Density, g/cm^3	1.18	1.13
Energy dissipation ratio, %	33.4 ± 2.4	99.5 ± 3.7
Flexural stiffness, kN/mm	1.08 ± 0.11	0.0167 ± 0.0064
Response time, ms	0.48 ± 0.12	~2000
Maximum force at break, kN	1.76 ± 0.78	0.109 ± 0.059
Maximum displacement, mm	1.57 ± 0.31	27.3 ± 3.1
Maximum velocity without failure, m/s	3.45	3.41
Maximum energy without failure, $mV_{ini}^2/2$, J	1.99	1.95
Minimum velocity with failure, m/s	3.50	3.62
Energy absorption with failure, $mV_{ini}^2/2 - mV_{res}^2/2$, J	1.95	2.19

To occupy the whole plane, we model the concentric structure as concentric hexagons (Fig. 1b). Finally, the rotating plywood microstructure is reported for its outstanding fracture tolerance in stomatopod (Weaver et al., 2012), teleost scales (Bigi et al., 2001), and human teeth (Yamamoto et al., 2000). The constructing units of these microstructures are summarized in Fig. 1, based on which the volume fractions of the soft phase are evaluated as (see supplementary material for details)

$$V_{soft}^{Layer} = \frac{t}{a+t}, \tag{1}$$

$$V_{soft}^{B\&M} = 1 - \frac{\rho a^2}{(a+t)(\rho a+t)}, \tag{2}$$

$$V_{soft}^{Bone} = \frac{(2N^2+5N-1)at + (2N^2+3N-1/2)t^2}{2(N^2+N)a^2 + (4N^2+5N-1)at + (2N^2+3N-1/2)t^2}, \tag{3}$$

$$V_{soft}^{Cross-Lamellar} = 1 - \frac{abc}{(a+t)(b+t)(c+t)}, \tag{4}$$

$$V_{soft}^{Plywood} = \frac{t^2+2at}{(a+t)^2}, \tag{5}$$

where a, b, c, and t are the geometric parameters shown in Fig. 1, ρ is the aspect ratio of the brick, and N is the concentric layer number. With Eq. (1-5), the geometric parameters of the microstructures are calculated such that the soft volume fraction of all the microstructures are 0.25, except that of the concentric hexagonal structure is 0.50 (since bone has a greater volume fraction of soft phase (Zhang et al., 2011)). These microstructures are then printed into $18 \times 88 \times 8\,\text{mm}^3$ beams using a commercial Objet Connex260 3D printer (Stratasys corporation). The printer is capable to print multi-materials simultaneously and has a print precision of 30 µm in the layer direction and 43 µm (600DPI) in the other two directions. The two base materials are a soft rubbery polymer Tango Plus, and a stiff glassy polymer VeroWhite (properties provided in Table 1).

2.2. Dynamic three-point bending tests

The low velocity dynamic tests are performed using a modified split Hopkinson pressure bar (SHPB) (Jia et al., 2018b) with impact velocities in the range of 2~12 m/s (Fig. 2). The impact velocity is controlled by high pressure air. The bending span is 72 mm, corresponding to a span to depth ratio of 4 (ensure small end effect in the middle), and the impactor has a mass of 335.26 g. The impact duration is then recorded by a high-speed videoing system (Photron SA1.1) (Fig. 2c) with 15,000 frames per second. Displacement and velocity histories are then calculated by digital image correlation (DIC) using the commercial software VIC-2D (Correlated Solution Inc.). The relation between impact velocity and flexural strain is formulated as $\dot{\varepsilon}_f = 6Vd/L^2$ (Standard, 2010), where d is the depth, L is span of the beam, and V is the impact velocity. The impact speed 2~12 m/s corresponds to $\dot{\varepsilon}_f$ of 4.2~25.0 s^{-1}, in which range the change of polymer performance is not very significant (Roland, 2006). In our experiment, the performances in the viscoelastic regime, such as flexural stiffness and energy dissipation are obtained by impact specimens at ~3 m/s for three trials. The critical values related to failure are found by gradually increasing the impact velocity until the failure of the specimen. In finding the critical parameters of the bioinspired microstructures, one specimen is tested at each velocity. At least 8 specimens are tested for each microstructure.

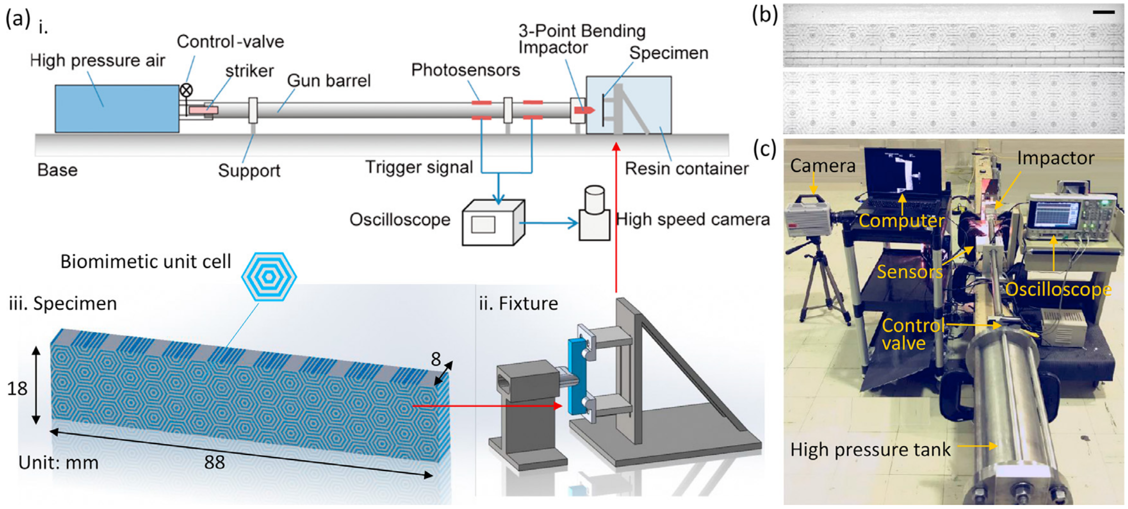

Fig. 2. Experiment setup. (a) Schematic of the modified split Hopkinson pressure bar system (SHPB), the fixture, and the specimen. (b) Specimens fabricated by 3D printing, top shows a hybrid beam with three layers: a hard layer, a concentric hexagonal layer, and a brick and mortar layer, bottom shows the concentric hexagon microstructure with staggered hierarchy. The scale bar represents 5 mm. (c) Photograph of the SHPB, pictured are the high press tank, gun barrel, and the high-speed videoing system.

2.3. Strain field visualization and dynamic performance characterization

The strain fields are obtained experimentally by DIC analysis. Fig. 3a demonstrates the deformation history of the concentric hexagonal specimen impacted at 4.2 m/s. From the recorded videos, the deflection, velocity, and force histories can be calculated, which are further used to characterize the dynamic parameters (Fig. 3b). Dynamic performances like flexural stiffness, energy dissipation, and response time are evaluated at a relatively small impact velocity (viscoelastic regime, before damage takes place). For example, energy absorption is estimated as the kinetic energy loss

$$E_{ab} = \frac{1}{2}mV_{ini}^2 - \frac{1}{2}mV_{res}^2, \tag{6}$$

where V_{ini} and V_{res} are the initial and residual velocity of the impactor, m is the mass of the impactor. Referring to the definition of loss tangent used to measure dissipation under sinusoidal dynamic loadings (defined as the ratio between the dissipated energy and maximum stored energy) (Lakes, 2009), the energy dissipation ratio during an impact event is calculated as $\eta = 2E_{ab}/mV_{ini}^2$. In addition, the response time is evaluated as the time required for the specimen to totally push the impactor back at a certain incident energy.

A specimen's resistance of failure under impact loading can be evaluated by critical velocity, critical force (analogy to strength), and critical energy (analogy to toughness). Since the exact critical values are impractical to draw, we bound them experimentally by two values – a maximum value before perforation and a minimum value that perforates the specimen (Fig. S9). Note that the critical energy is evaluated by the incident energy, $mV_{ini}^2/2$.

3. Results

3.1. Constituent mateial performance

The dynamic performance of the constituents is summarized in Table 1. The hard phase (VeroWhite) is a glassy polymer which is stiff and has low energy dissipation (short response time), but it's brittle at dynamic loading conditions (flexural strain at failure = 0.033). By contrast, the soft phase (Tango Plus) shows the typical properties of a rubber – it is soft and flexible, has high energy dissipation, but lacks stiffness and strength (long response time). Fig. 4 shows that the VeroWhite specimen fragments at impact velocity V_{ini}=3.5 m/s, while Tango Plus snaps through the fixture at V_{ini} =3.62 m/s. Both materials are not tough, with critical energy around 2 J. Realistic applications often require materials to be: 1) flexible and fast response (soft robotic), 2) stiff and dissipative (wave attenuation), 3) strong and tough (general requirement), for which both the constituents are far from qualified. One promising approach to solve this dilemma is architected microstructure design as we'll discuss next.

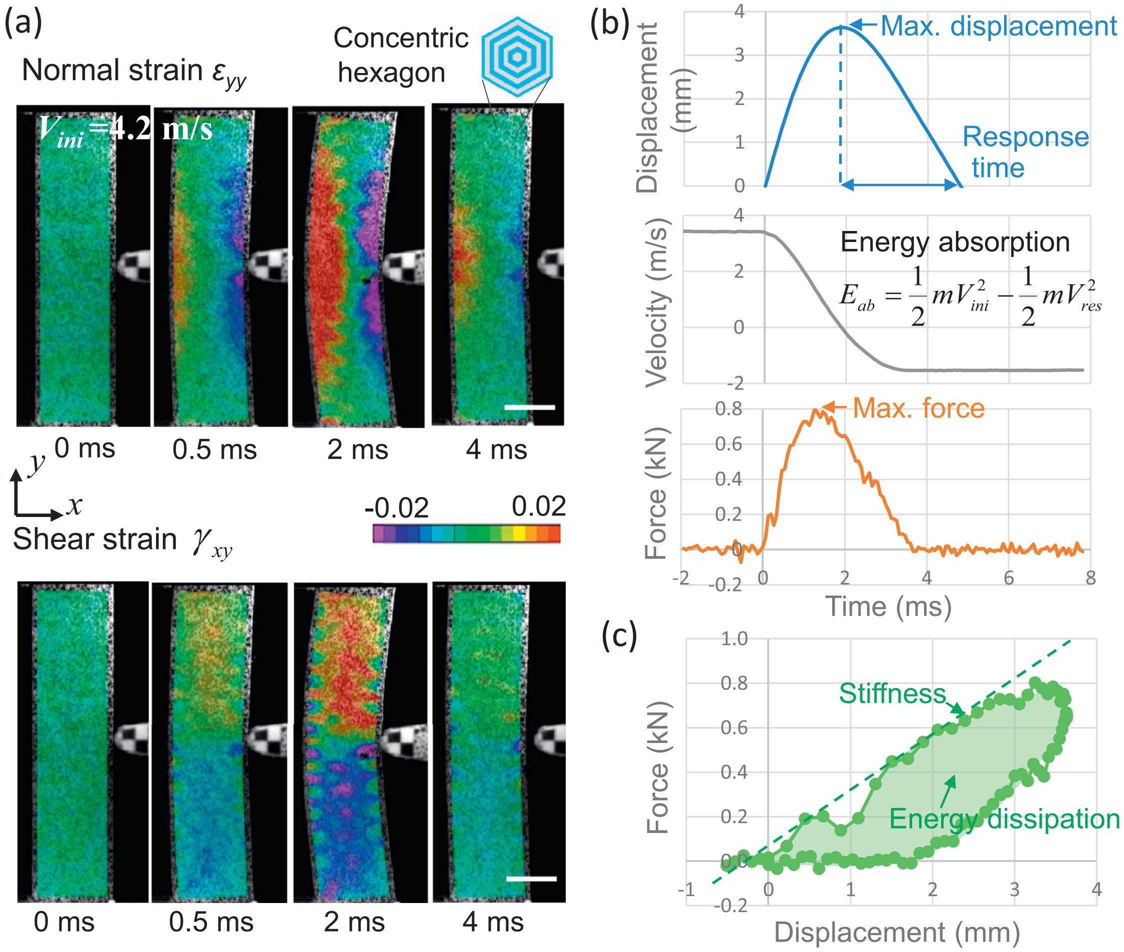

Fig. 3. Digital image correlation (DIC) results of the concentric hexagon specimen (bone osteon inspired) impacted at 4.2 m/s. (a) Snapshots of the normal and shear strain field during the impact process. Scale bars: 1 cm. (b) The displacement, velocity, and reaction force histories of the impactor. (c) The force-displacement curve. Highlighted are the definition of maximum displacement/force, flexural stiffness, response time, and energy dissipation.(For interpretation of the references to color in this figure legend, the reader is referred to the web version of this article.)

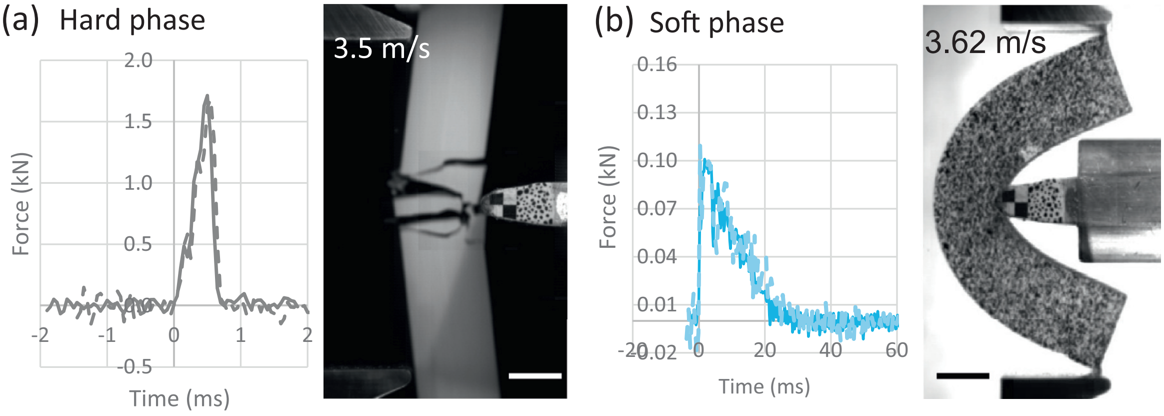

Fig. 4. The force histories of the hard phase (VeroWhite) and the soft phase (Tango Plus) under impact. (a) The VeroWhite specimen fail by fragamentation at an incident velocity of 3.50 m/s. (b) The Tango Plus specimen snaps through the fixture at an incident velocity of 3.62 m/s. Scale bars: 1 cm.

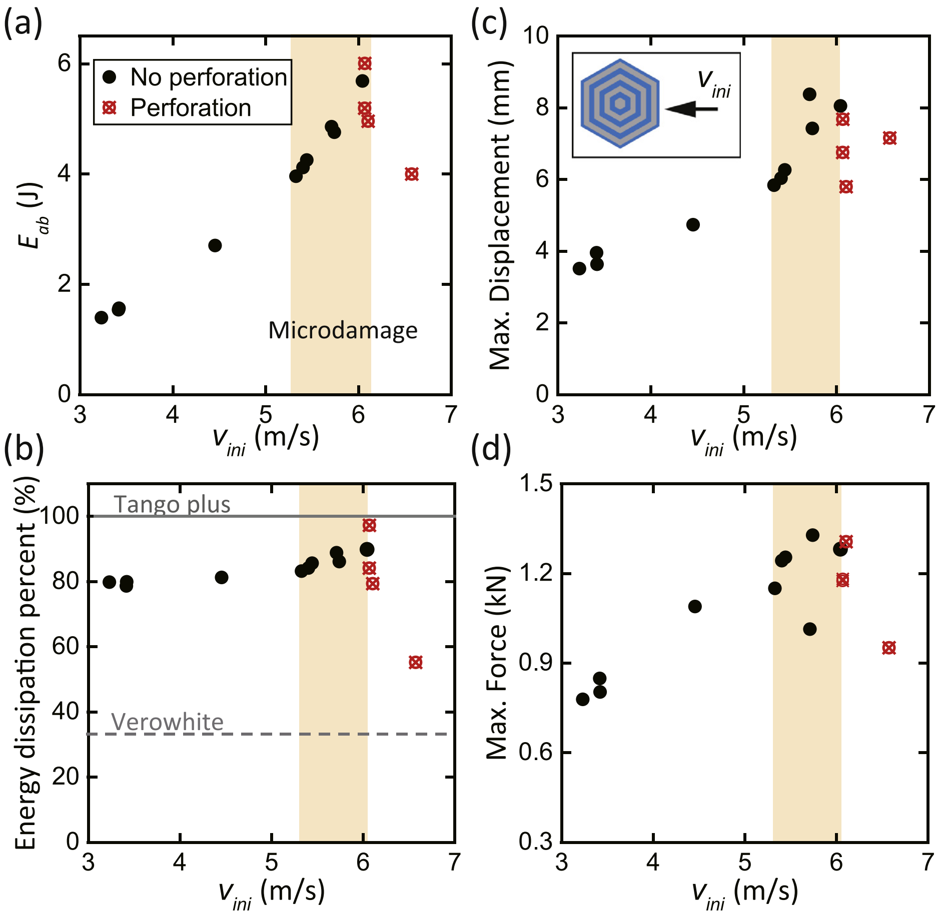

Fig. 5. Dynamic performance of the concentric hexagonal architected beam. (a-d) show the energy absorption ($E_{ab} = mV_{ini}^2/2 - mV_{res}^2/2$), energy dissipation ratio, maximum displacement, and maximum force, respectively. The shaded areas highlight the velocity range where micro-damages are observed. The inset in (c) shows the impact direction with respect to the unit cell. The red crossed symbols reperesents the perforation of the specimen.

3.2. Biomimetic microarchitecture results

3.2.1. Concentric hexagonal microstructure

The dynamic performance of the concentric hexagonal architected beam at impact speed $V_{ini} = 3.2 \sim 6.6$ m/s is shown in Fig. 5. The energy absorption $= mV_{ini}^2/2 - mV_{res}^2/2$ is equal to the energy dissipation before perforation, and is approximately the fracture energy (residual kinetic energy is small) when the specimen breaks. Fig. 5a shows that the specimens stay intact when $V_{ini} \leq$ 6.04 m/s (black solid points), and break at $V_{ini} \geq$ 6.10 m/s (red crossed points), which narrows the critical velocity to the range of 6.04~6.10 m/s, about 75% higher than the constituents. The critical energy required to break the specimen is in the range of 6.12~6.26 J, more than ~3 times that of the constituents.

Table 2 summarizes the dynamic performance of the concentric hexagonal structure, which is 140% more dissipative, 270% more flexible, and 200% tougher than VeroWhite, with only 25% sacrifice in strength and 75% sacrifice in stiffness. Compared to Tango Plus, the architected design is 15 times stiffer, 10 times stronger, 2 times tougher, and response 1000 times faster, with less than 20% reduction in the energy dissipation. Such remarkable improvements make the concentric hexagonal microstructure a competitive candidate of responsive, dissipative, stiff, and strong materials.

3.2.2. Brick and mortar microstructure

The dynamic three-point bending response of the brick and mortar microstructured beam is summarized in Fig. 6. Compared to the concentric hexagonal microstructure, it possesses a larger critical impact velocity (7.05 m/s), higher energy dissipation (88.5%), and more significant microdamages (Fig. 6e). The maximum force and flexibility are about the same, but the response time is 19% longer and the flexibility is 41% smaller. Moreover, the brick and mortar structure is highly anisotropic, i.e., the direction parallel to the hard plates shows 80% less fracture energy than the perpendicular direction.

Table 2
Performance summary of the architected beams with different microstructures.

Microarchitectures					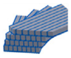	
Energy dissipation percentage, %	80.0 ± 0.6	88.5 ± 0.5	89.1 ± 1.2	93.8 ± 0.1	45.5 ± 0.3	84.0 ± 0.11
Flexural stiffness, kN/mm	0.265 ± 0.014	0.344 ± 0.018	0.108 ± 0.021	0.094 ± 0.005	0.740 ± 0.060	0.488 ± 0.030
Response time, ms	2.87 ± 0.32	3.40 ± 0.10	6.41 ± 0.40	9.20 ± 0.51	1.53 ± 0.07	2.13 ± 0.11
Maximum force at break, kN	1.30 ± 0.01	1.30 ± 0.03	1.05 ± 0.27	1.07 ± 0.11	1.45 ± 0.05	1.47 ± 0.04
Maximum displacement at break, mm	5.80 ± 0.32	3.35 ± 0.05	9.39 ± 1.13	12.67 ± 2.21	2.70 ± 0.27	2.96 ± 0.21
Maximum velocity without failure, m/s	6.04	7.05	8.58	8.69	3.41	4.04
Maximum energy without failure, J	6.12	8.33	12.33	12.67	1.95	2.73
Improvement compared to VeroWhite	207.6%	318.6%	519.2%	536.4%	−1.9%	37.4%
Minimum velocity with failure, m/s	6.11	7.32	8.80	8.74	3.56	4.16
Minimum energy with failure, J	6.26	8.98	12.98	12.80	2.12	2.90

Note: The energy dissipation percentage, flexural stiffness, and response time are evaluated at an impact velocity of 3 m/s (viscoelastic regime, before damages take place). The maximum and minimum values refer to the maximum and minimum results obtained in our experiments.

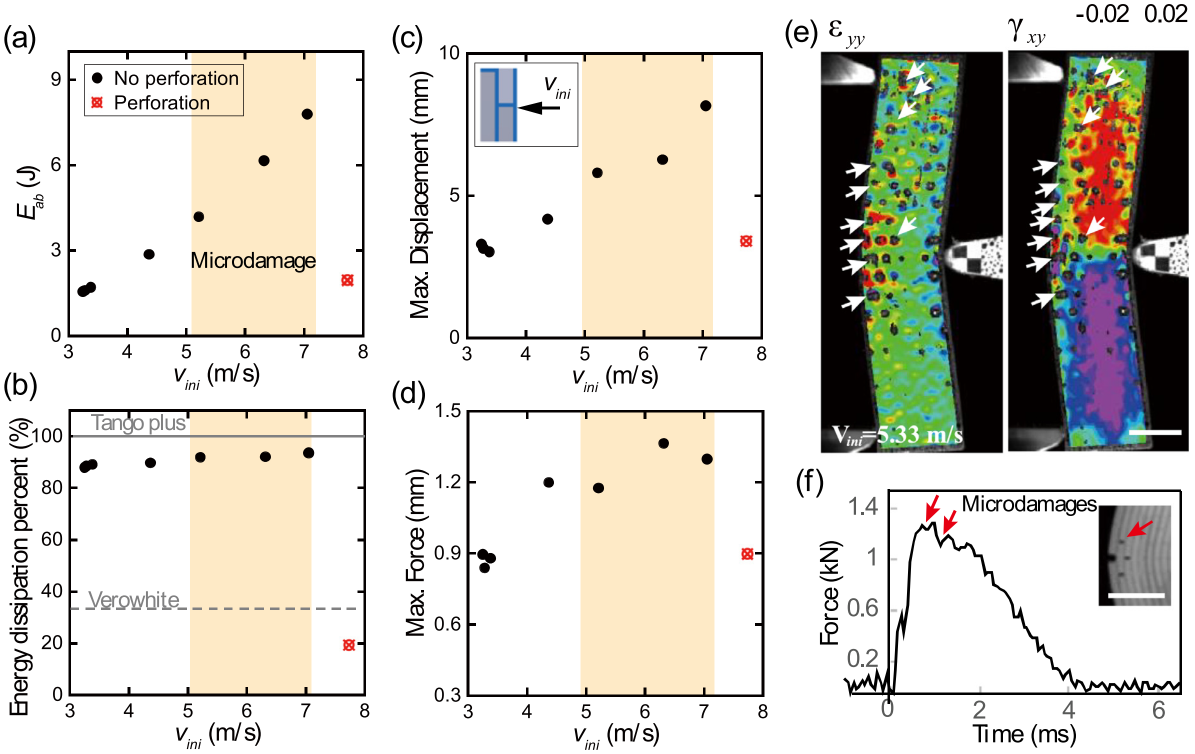

Fig. 6. Dynamic performance of the brick and mortar architected beam. (a-d) show the energy absorption, energy dissipation, maximum displacement, and maximum force, respectively. The shaded areas indicate the velocity range with micro-damages. (e) The strain field at $V_{ini} = 5.33$ m/s, where white arrows indicate sites of microdamage. (f) The force history, where the force drops correspond to micro-cracking. Scale bars: 1 cm.

3.2.3. Layer microstructure

For the layer microstructure, two volume fractions of the soft material are studied (with $V_{soft} = 0.25$ and 0.50 represent highly mineralized and intermittent mineralized situations). Fig. 7a shows that the layered beams do not break at $V_{ini} = 8.6$ m/s, having a critical energy > 12 J, over 5 times greater than the consitutients. As expected, a higher volume fraction of the soft phase makes the beam slightly more flexible and dissipative. The influence of V_{soft} is small, verifying the dominant role of the architecture. Moreover, extensive shear deformations instead of microdamages are observed in the layered specimen prior to failure, making them more reusable. However, the shear deformations reduce the stiffness significantly, performing only 10% stiffness of the hard phase and 27% of the brick and mortar microstructure. The force vs displacement curve of the layer microstructure is shown in Fig. 8 in comparion with other microstructures. Results show the layer structure exhibtis the maximum hysteresis before damage and the maximum work of fracture, validating its high dissipation and high toughness.

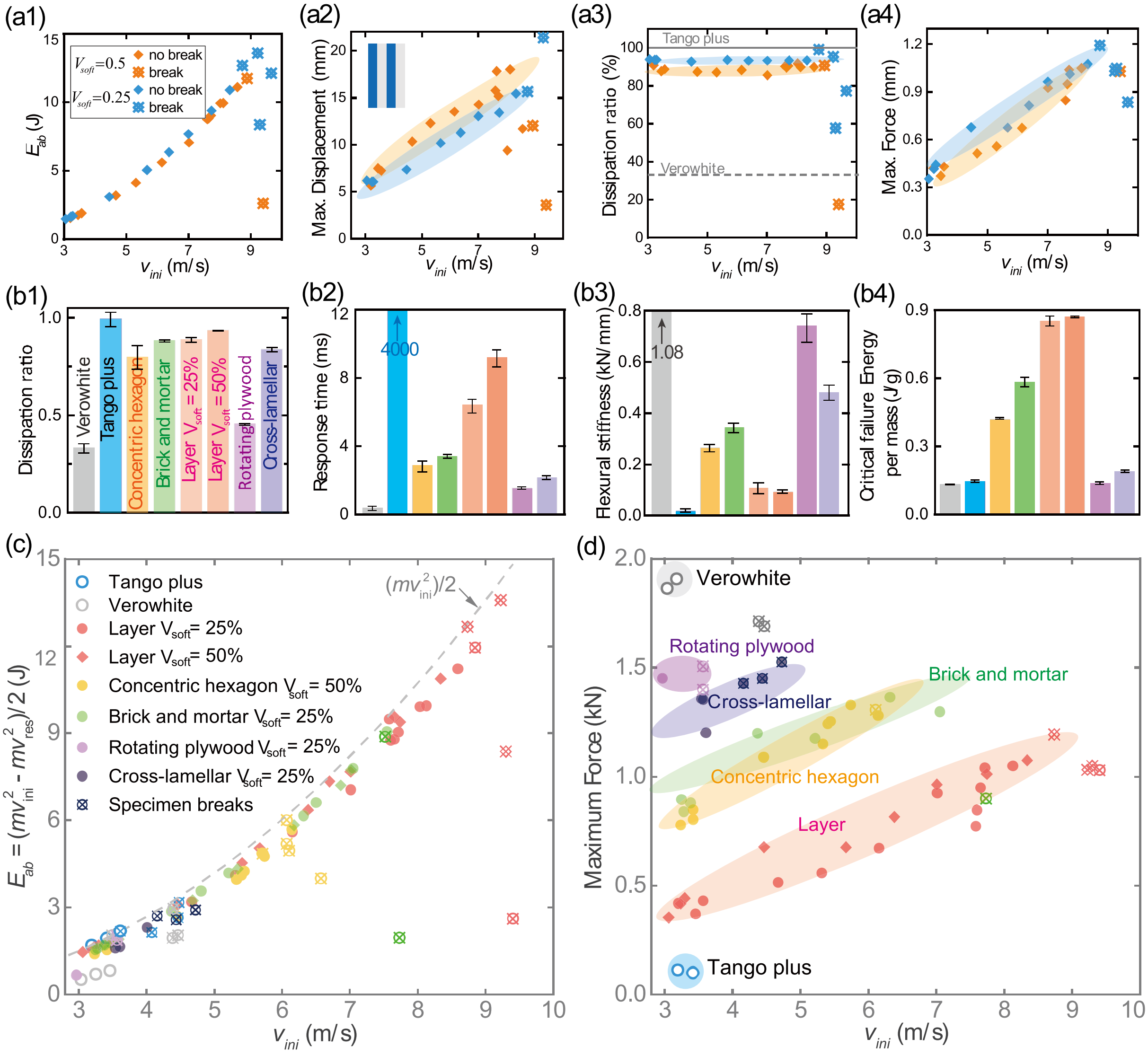

Fig. 7. (a1-a4) Dynamic performance of the layered beam. (b1-b4) Summarized energy dissipation, response time, stiffness, and toughness of the architected beams. (c) and (d) show the energy absorption and maximum force as functions of incident velocity for different microstructures. (For interpretation of the references to color in this figure legend, the reader is referred to the web version of this article.)

3.2.4. Rotating plywood and cross-lamellar microstructure

The results of the rotating plywood microstructure and cross-lamellar microstructure are also provided in Table 2 and Fig. 7b-d for comparison. Both the rotating plywood and cross-lamellar microstructure show high stiffness and fast response, but low flexibility and toughness. The fracture energy of the cross-lamellar is 50% greater than that of the hard phase. This result is consistent with the 85% improvement reported in a drop tower test (Gu et al., 2017b). Unexpectedly, the rotating plywood structure does not exhibit significant critical energy improvements, unlike the super impact survivability of its biomaterial counterpart (Weaver et al., 2012). This inconsistency might come from three aspects. First, the loading condition, our specimen is printed into a beam and tested in three-point bending. While for stomatopod, it's in the middle layer which works synergistically with the outer impact region and inner striated region (Weaver et al., 2012). Second, the dactyl club has a curvy 3D shape, which plays an essential role in maximizing the carack arresting ability of the rotating plywood microstructure. Third, the constituent materials and length scale might also account for such discrepency. Nevertheless, here we show that the rotating plywood microstructure does have advantages over other microstructures – high stiffness and low energy dissipation (Fig. 7b), which are critical for the stomatopod to break its heavily mineralized prey and in teeth to break down food.

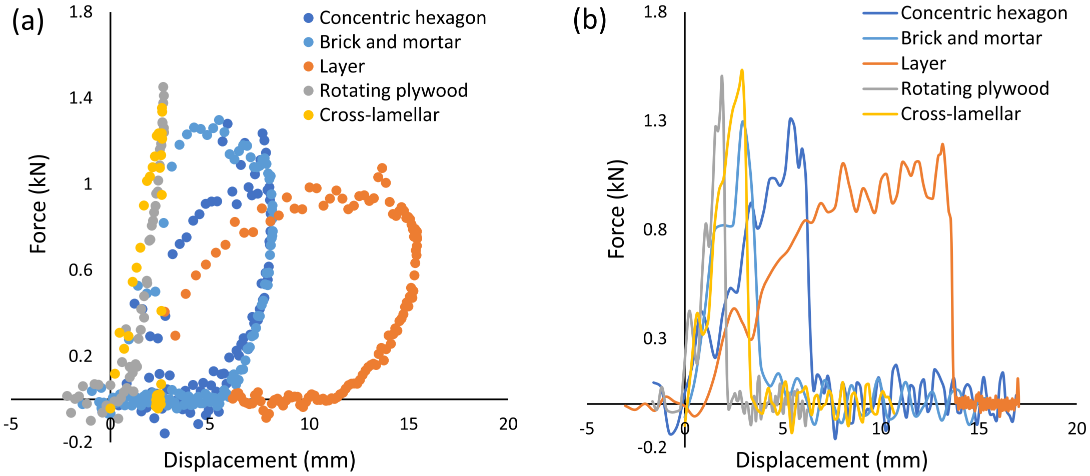

Fig. 8. Force vs displacement curves of the five microstructures (a) at maximum impact velocities before specimens break and (b) at minimum impact velocities that break the specimens. (For interpretation of the references to color in this figure legend, the reader is referred to the web version of this article.)

3.3. Comparison between different biomimetic microstructures

In summary, the layer structure has the highest dissipation and critical energy, but has a relatively long response time and a low stiffness. The structural simplicity and high toughness make it an essential component for more complex material architectures. The rotating plywood and cross-lamellar structure are stiff and responsive, but less tough. By contrast, the concentric hexagonal structure and the brick and mortar structure show a better balanced performance, having no significant shortcomings. Thus, they are more robust microstructures (Currey, 1999), which is an important reason why they're quite common in nature.

The distinct performance of different microstructures is highly related to their deformation and failure mechanisms. Fig. 9a-f demonstrate the strain fields of the architected beams, which show highly localized deformations compared to the homogenous beam. These localized strains facilitate distributed micro-damages and prevent catastrophic failure. Specifically, the concentric hexagon structure shows localized shear strains (Fig. 9b), while the brick and mortar microstructure shows localized normal strains (Fig. 9c). By contrast, the layer microstructure present extensive shear deformations, suggesting a shear dissipation mechanism (Fig. 9d). Moreover, the cross-lamellar and the rotating plywood microstructure exhibit small strains at failure. Fig. 9f suggests that the rotating plywood microstructure can't effectively accommodate deformations into the soft material. Thereby, it breaks at a small deflection. The small deformations in the soft phase also explains the low dissipation and high stiffness of the rotating plywood microstructure. Note that although the rotating plywood structure cannot accommodate large deformations properly, it does not exclude its crack arresting capability. Our compact tension fracture tests have verified its outstanding crack arresting ability, which has a "J" shaped rising *R*-curve (Jia and Wang, 2019). As such, the rotating plywood structure is preferable in regions where deformations are small, but high stiffness and crack arresting ability are required. Examples include teeth (Yamamoto et al., 2000), teleost scales (Bigi et al., 2001), and the center layer of stomatopod dactyl club (Weaver et al., 2012).

The energy absorption ability of different microstructures is greatly related to their fracture pattern, as shown in Fig. 9h-l. For instance, microcracking is found in microstructures including the concentric hexagon, brick and mortar, and rotating plywood structure. Crack bridging is widespread in the concentric hexagon, brick and mortar, and layer microstructures, produced by alternating soft and hard materials. By contrast, crack branching is only found in the rotating plywood microstructure. These experimental results suggest that architectures with extensive microcracking and bridging (which expand the fracture process zone more effectively) typically possess higher fracture energies than that of crack deflection and branching (which have small influence on the fracture process zone). We will further discuss these toughening mechanisms in section 4.2.

3.4. Comprehensive characterization of the material performance

So far, we've used more than six parameters to characterize the performance of the micro-structured beams. Although such descriptions give a detailed picture of the mechanical performance, it is cumbersome. The usage of one or fewer parameters is preferable in material selection. To satisfy such needs, we first use radar plots to give an intuitive visualization of the overall performance (Fig. 10a). Based on the radar plot, one straightforward way for qualitatively evaluating the overall performance is the area of the enclosed polygon. Thereby, a comprehensive parameter is quantitatively calculated by multiplying the normalized flexibility, dissipation ratio, strength, toughness, and response rate. Fig. 10b summarizes the normal-

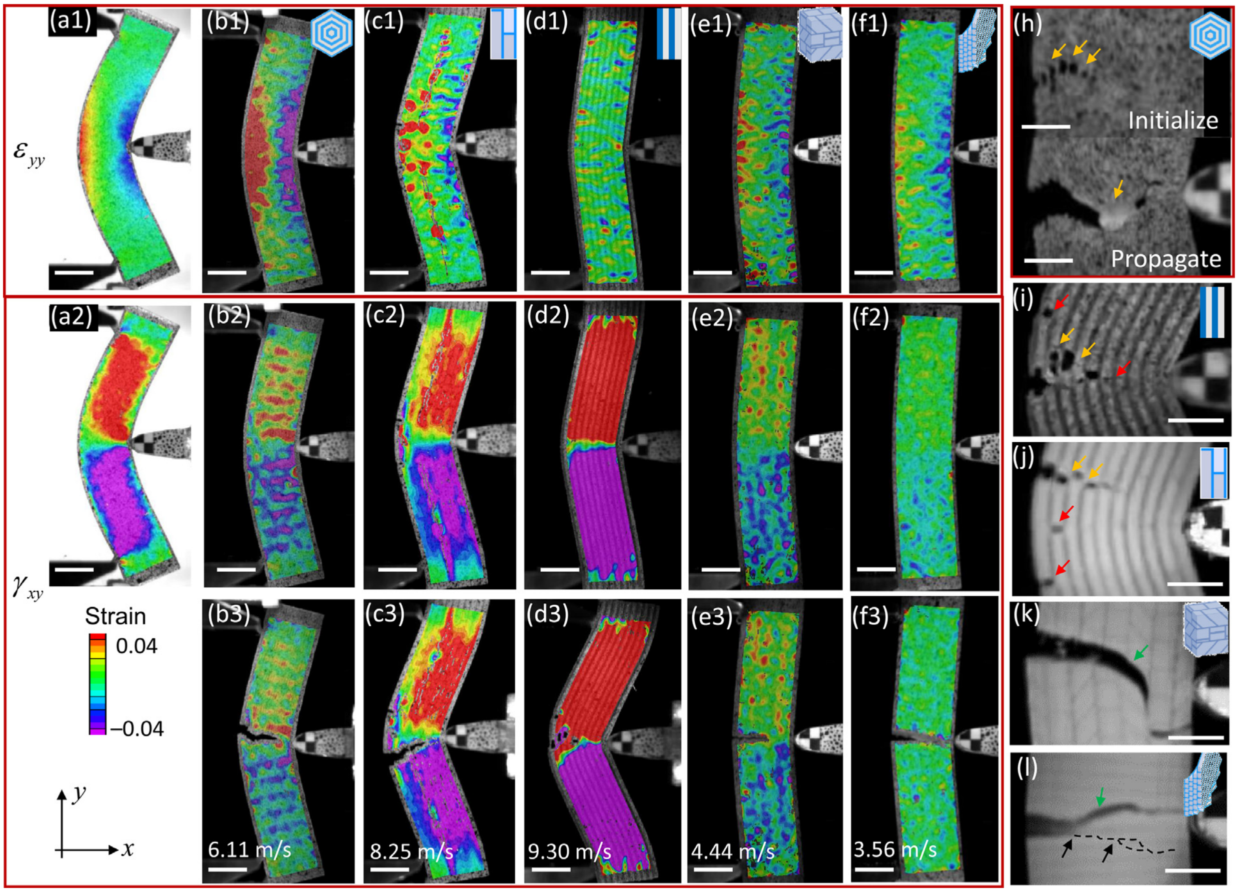

Fig. 9. The deformation and crack patterns of different architected beams. (a1-f1) normal strains and (a2-f2) shear strains without failure, (b3-f3) shear strains at failure. The corresponding impact velocities are marked on the bottom. (h-l) highlight the crack patterns of different microstructures. The red, yellow, green, and black arrows mark the locations of micro-cracking, crack bridging, crack deflection, and crack branching, respectively. The dashed line in (l) marks the secondary cracks. Scale bars in (a-f) represent 1 cm, in (h-l) represent 5 mm. (For interpretation of the references to color in this figure legend, the reader is referred to the web version of this article.)

ized results, where an arbitrary unit can be used since we're only interested in the ratio. Results show that the architected microstructure design (shadowed areas) possess a better overall performance than the constituents (dashed lines). Note that the parameter defined above is suitable for applications like soft actuators and wearable electronics, where flexibility and fast response are of great importance. By contrast, in helmet design, structural components, and telescopes, stiffness is of great importance. In such scenarios, a performance parameter considering stiffness, strength and toughness can be proposed similarly (Jia et al., 2019).

Furthermore, once given specific applications, the concept of material indices proposed by Ashby is competent to the material characterization (Ashby, 2016). For example, in the strength-limited design of springs for maximum stored elastic energy per unit mass, the material index can be derived as $\sigma_f^2/K\rho$, where σ_f, K, and ρ are the flexural strength, stiffness, and effective density, respectively. For a beam vibration problem, an objective of minimum flexural excitation at external driving force gives the material index $\eta K^{1/2}/\rho$, with η being the dissipation ratio. The results of these material indices are presented in Fig. 10c and d, which show that the layered microstructure and the cross-lamellar microstructure should be selected for maximum stored elastic energy and minimum flexural excitation beam design, respectively. More material indices alike can be found in (Ashby, 2016), which provide powerful tools in the selection of material architecture.

3.5. Hierarchical designs

As discussed earlier, hierarchies spanning multiple length scales are important features of biomaterials. With a self-similar hierarchy assumption (microstructures are the same at all hierarchical levels), Zhang and Gao have shown theoretically that hierarchical structures can improve toughness by orders. But at the same time, stiffness and strength will be sacrificed (Gao, 2006; Zhang et al., 2011). Another study by Lakes gives a similar prediction: the exponentially increased strength of a hierarchical honeycomb at an increasing level of the hierarchy is largely at the expense of stiffness (decreases

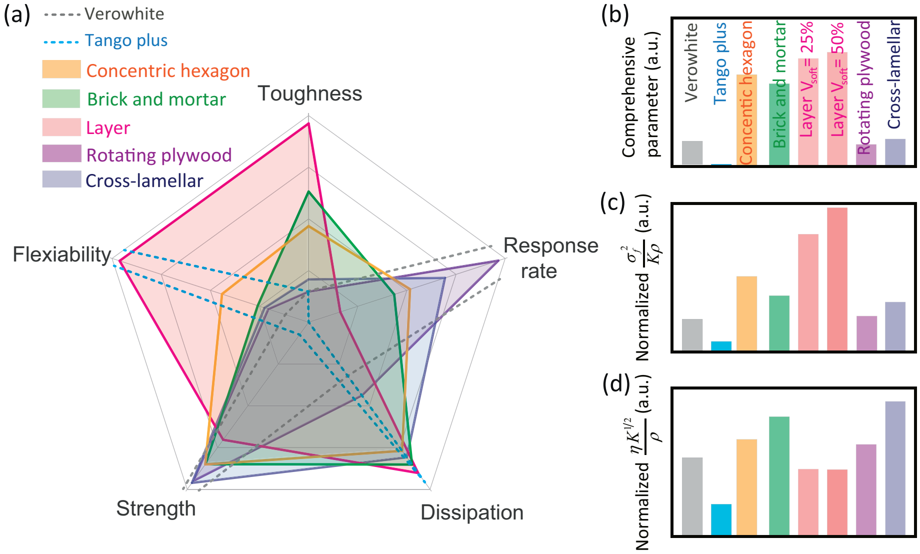

Fig. 10. Comprehensive characterization of the bioinspired architected beams. (a) Visualization of the material performance in a radar plot. All the values are normalized. The material performance characterized by (b) the comprehensive parameter (analogy to the area of the polygon), (c) material index $\sigma_f^2/K\rho$, and (d) material index $\eta K^{1/2}/\rho$. (For interpretation of the references to color in this figure legend, the reader is referred to the web version of this article.)

exponentially) (Lakes, 1993). Besides these self-similar results, we've recently designed hierarchical honeycombs with second order microstructures different from the first order, by which simultaneously improved stiffness and strength are obtained (Chen et al., 2016). Thereby, different (more ideally, optimal) microstructures at different hierarchical levels appears to be essential for architected materials to achieve simultaneously improved stiffness, strength, and toughness. Here, we study the role of hierarchy by replacing the hard phase of the concentric hexagonal structure with two types of second order microstructures. The first design mimics the lamellar microstructure of the bone (Fig. 11a), and the second hierarchical design is inspired from the staggered structure of a collagen fibril (Fig. 11c). Note that the volume fraction of the soft material remains the same (all geometric sizes are provided in the Supplementary Material).

The mechanical performances of the hierarchical designs are then evaluated from three orthogonal directions (Fig. 11e-h), showing improved energy dissipation, failure force, and fracture energy with small stiffness loss. Specifically, the improvements of the staggered hierarchy reach ~26% energy dissipation, ~200% maximum displacement, ~60% failure force, and ~100% fracture energy. This simultaneously improved strength and toughness is different from the self-similar predictions, verifying that proper microstructures at different hierarchical levels are important to improve stiffness, strength, and toughness simultaneously (Chen et al., 2016).

Next, we study the mechanism of the improved strength and toughness. In the hierarchical designs, deformations are localized at a finer length scale confined by the second order microstructure. Fig. 11d shows that these deformations evolve into extensive microdamages which is not observed in the original design (Fig.9b). Microcracking prevents catastrophic damage and dissipates extra energy, making the material stronger and tougher. Moreover, the staggered hierarchical design shows an inclined crack path (Fig. 11e), corresponding to the “flexural shear crack” in concrete beam design (Devadas, 2003). Interestingly, while “flexural shear cracks” are catastrophic and are considered unfavorable in civil engineering, they are advantageous in the proposed architected beams. This contradiction can be explained by the difference in the constituent materials – the concrete beam has a brittle matrix, while our hierarchical beam has a compliant matrix. Hence, in our case, an inclined shear crack penetrating softer matrix is more progressive, and a longer crack path makes it tougher.

3.6. Hybrid beam designs

So far, all the beams are produced by distributing the same microstructure, which correspond to a homogenous design strategy if the microstructures are sufficiently small. By contrast, another approach – the gradient design strategy, is intrinsically heterogeneous and are also common in both engineering materials (Wang and Nakamura, 2004) and biomaterials. Examples include fish scale (Bruet et al., 2008; Wang et al., 2009b), teeth (Lawn et al., 2010), snail shell (Yao et al., 2010), and stomatopod clubs (Weaver et al., 2012). Following similar ideals, four hybrid gradient designs (simplified to have three layers) are proposed (Fig. 11). Design 1 and design 2 use a strategy similar to stomatopod (Weaver et al., 2012), where the first hard layer prevents penetration, the second layer is crack tolerant serving as a crack capturer, and the third layer uses a microcrack mechanism to dissipate as much impact energy as possible. Design 3 and design 4 are based on the layer microstructure, with a concentric hexagon and a VeroWhite layer for reinforcement respectively. Note that because of the size

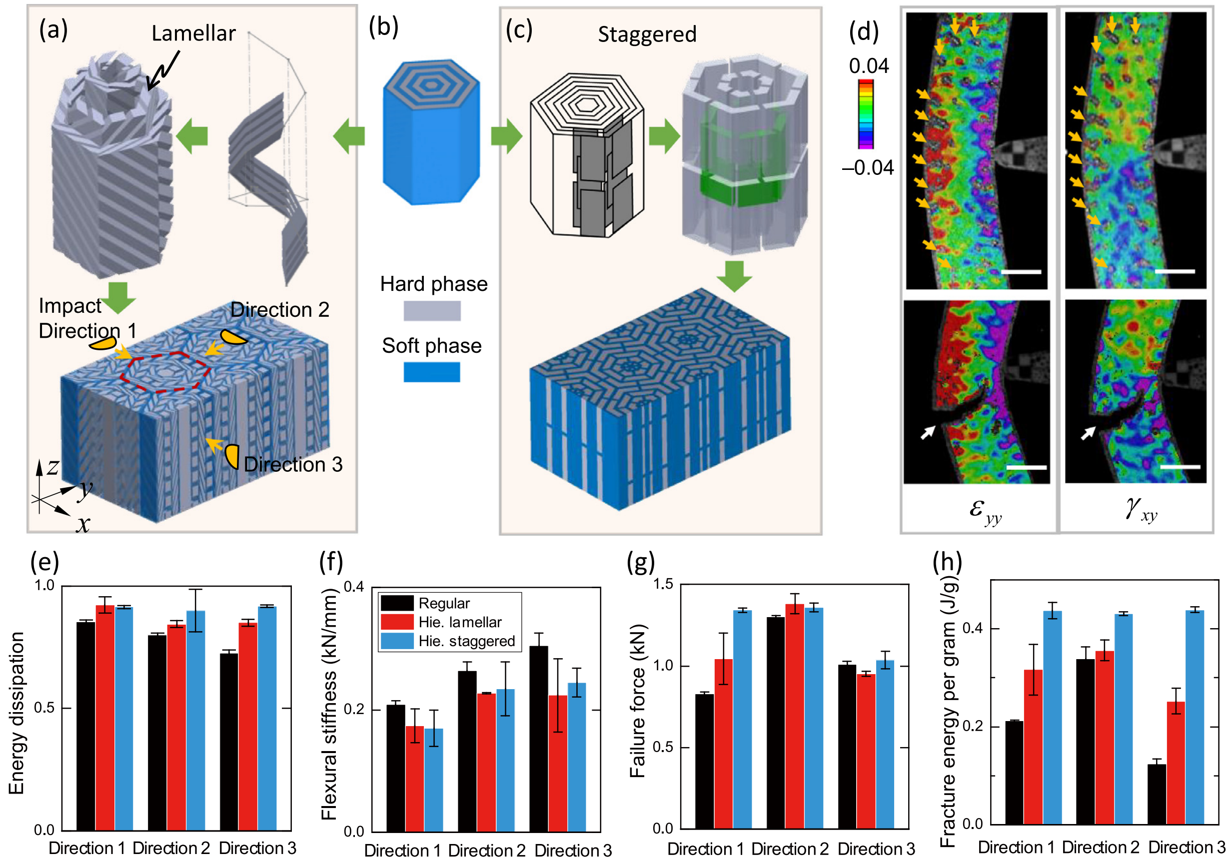

Fig. 11. The hierarchical designs. (a) The lamellar hierarchical design, (b) the original concentric unit cell, and (c) the staggered hierarchical design. The impact directions are defined in (a). (d) Top and bottom show the strain fields before and after damage, respectively. The yellow arrows highlight the locations of micro-damages. The white arrows show the "flexural shear crack". (e-h) show the effect of hierarchical design on the material performance. Scale bars: 1 cm.

Table 3
Dynamic performances of the architected beams with hybrid microstructures.

	Design 1	Design 2	Design 3	Design 4
Energy dissipation percentage, %	71.5 ± 6.2	70.7 ± 4.7	90.6 ± 0.2	81.0 ± 1.6
Flexural stiffness, kN/mm	0.49 ± 0.06	0.13 ± 0.3	0.12 ± 0.01	0.17 ± 0.04
Response time, ms	1.87 ± 0.11	3.73 ± 0.2	7.73 ± 0.13	4.53 ± 0.53
Maximum force at break, kN	1.71 ± 0.12	1.23 ± 0.02	0.90 ± 0.12	1.20 ± 0.08
Maximum displacement, mm	6.22 ± 0.76	14.60 ± 0.99	12.41 ± 0.75	17.15 ± 0.98
Maximum velocity without failure, m/s	6.19	7.52	8.60	9.35
Maximum energy without failure, J	6.42	9.47	12.41	14.65
Improvement compared to VeroWhite	222.5%	375.8%	523.3%	641.0%
Minimum velocity with failure, m/s	6.30	8.16	8.80	9.41
Minimum energy with failure, J	6.65	11.16	12.98	14.84

limit incurred by our 3D printer, the specimens do not have enough unit cells in a homogeneous point of view. Nevertheless, these designs serve to demonstrate the potential of hybrid designs.

Fig. 12 and Table 3 summarize the resultant dynamic performances. Compared to the single microstructure designs, hybrid designs further expand the material performances. For instance, compared to the concentric hexagonal microstructure, design 1 improves stiffness, strength, and response rate significantly, while the dissipation and flexibility are about the same. Moreover, design 3 shows a high energy dissipation, and design 2 is highly flexible. Overall comparisons between the constituents, bio-inspired architectures, hierarchical designs, and hybrid designs are summarized in Fig. 12f. Results demonstrate that hybrid designs successfully achieve toughness 7 times of VeroWhite, strength as high as VeroWhite, flexibility more than a half of Tango Plus, and an overall performance 12 times larger than VeroWhite. Importantly, compared to hierarchical designs (spanning multiple length scales), the hybrid designs (on one length scale) may be an alternative to obtain improved mechanical performance without placing too strict requirements on fabrication.

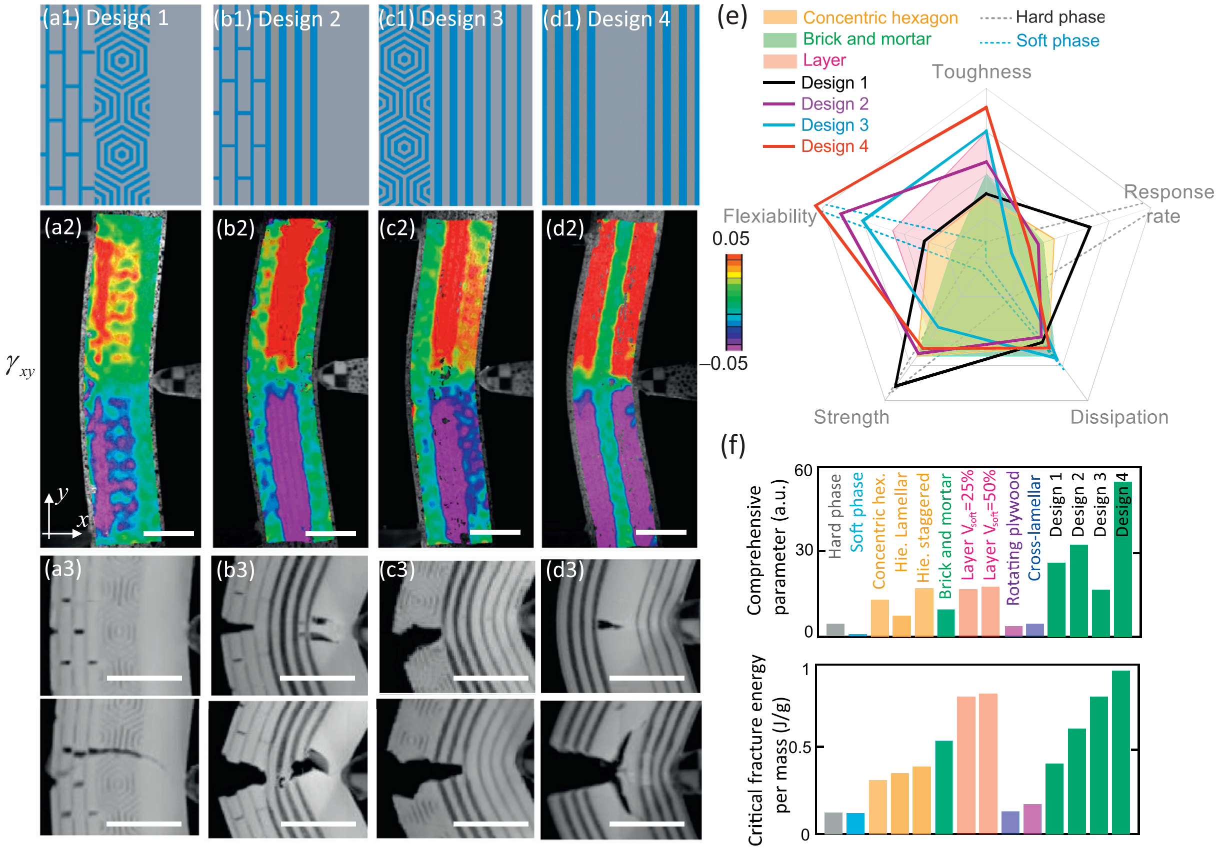

Fig. 12. Hybrid architected beam design. (a1-d1) show four hybrid beam designs, where the gray and blue color indicate the hard and soft phase, respectively. (a2-d2) show the shear strain field and (a3-d3) show the controllable crack locations and crack patterns in the hybrid design. (e) Radar plot demonstrating the hybrid beam performance compared to the single biomimetic microstructural beams. (f) Overall performance (top) and fracture energy per mass (bottom) comparison between different architected beam designs. Scale bars: 1 cm. (For interpretation of the references to color in this figure legend, the reader is referred to the web version of this article.)

Compared to the five structural elements and the hierarchical designs, hybrid microstructures give more controls over the strain field distribution. For instance, the shear strains can be accurately localized into either the front layer (the layer that contacts the impactor), the middle layer, the back layer, or a combination of these layers (Fig. 12a-d). As a result, both the location of crack initialization and the pattern of crack propagation can be controlled. For instance, the crack in design 2 and design 4 initiates from the back layer and the middle layer, respectively. Moreover, the propagating cracks slow down and blunt when encountering a soft layer (Supporting Video), which reduces the crack driving force significantly. Importantly, advantages of parent microstructures can be inherited to the child structures. For example, Design 1 inherits the stiffness of the mono-hard layer, the micro-cracking of the brick and mortar structure, and the shear resistance of the hexagonal structure, thus realizing better stiffness, strength and toughness. With expanded deformations and preferable damage patterns, the hybrid designs achieve a maximum critical energy improvement of 640%, 8 times of the improvement previously reported in 3D printed architected materials (Gu et al., 2017b).

4. Discussion

4.1. Breaking the performance tradeoffs with material architecture

The goal of the architected material design is to use material architecture to create material performance beyond that of bulk material. To demonstrate how effective material architectures are in expanding the material's property space, we plot all the proposed architecture designs in Ashby plots (Fig. 13) in comparison with the constituents and the rule of mixture results. The four subplots represent four objectives often raised in engineering materials: (a) stiff and strong, (b) strong and tough, (c) stiff and dissipative, (d) flexible and responsive. While many of these criteria are considered exclusive in bulk materials, quite remarkably, these goals are realized by material architecture designs. Compared to the rule of mixture

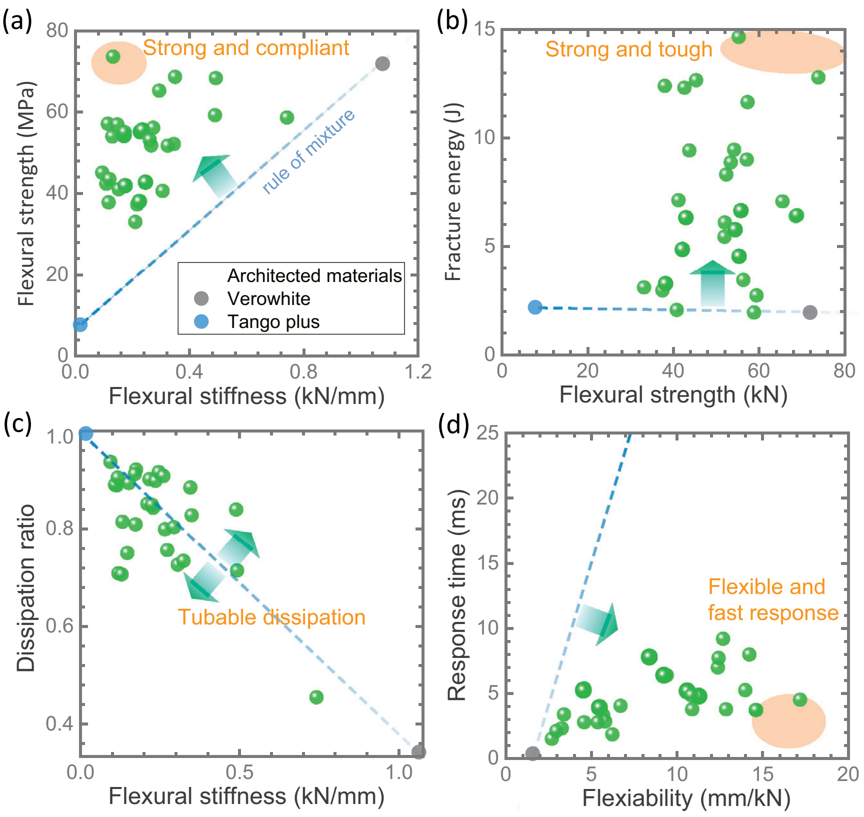

Fig. 13. Ashby plots demonstrating the role of material architecture in expanding the material property space. (a) Flexural strength plotted against flexural stiffness. (b) Fracture energy plotted against flexural strength. (c) Dissipation ratio plotted against flexural stiffness. (d) Response time plotted against flexibility. Each green point represents one architected beam design. The dashed lines represent the "rule of mixture" results, and the arrows highlight the desired trends of the architecture design. (For interpretation of the references to color in this figure legend, the reader is referred to the web version of this article.)

results, Fig. 13a-d show that proper architecture designs can (a) improve the strength at a specific stiffness, (b) improve the toughness at a specific strength, (c) tune energy dissipation at a certain stiffness, and (d) reduce the response time at certain flexibility. Importantly, the ingredients are quite simple – one hard phase and one compliant phase, where the broader performance space emerges from material architecture. As such, material architecture instead of the material constituents is the dominant factor. Therefore, the architecture designs proposed in this paper can be potentially adopted to other material constituents (like ceramics reinforce metals and graphene reinforced nanocomposites) and to smaller length scales (self-assembly and lithography).

4.2. Toughening mechanisms

When evaluating the performance of a specific material, toughness is often of special interest since it represents the material's ability against catastrophic failure. Many toughening mechanisms have been reported in architected materials including layered (Fratzl et al., 2007), staggered (Barthelat and Rabiei, 2011), twisted (Suksangpanya et al., 2017), and granular (Ovid'ko and Sheinerman, 2015) microstructures. Combining existing fracture models with the DIC strain field and in-situ videos, we will discuss the toughening effect of microcracking, crack deflection, crack bridging, and crack shielding. The dominant toughening mechanism will also be proposed.

Since the layer microstructure is the basis component of nearly all material architectures, let's first consider the situation when a crack is about to penetrate a layer structure with alternating stiff (modulus E_h) and compliant materials (modulus E_s). The relation between the J-integral at the far field (J_{far} crack driving force) and at the crack tip (J_{tip} decides whether a crack propagates) have been derived as (Fratzl et al., 2007)

$$J_{tip} = J_{far} \cdot (1 + f_{inh}), \tag{7}$$

where f_{inh} is the shielding factor, which depends on the relative thickness of the soft layer $\mu = t_h/t_s$ and modulus ratio $\eta = E_h/E_s$. Eq. (7) shows that if $f_{inh} < -1$, J_{tip} becomes negative, meaning that the crack will be stopped. With an equal thickness of the soft and hard layer ($t_h = t_s$) and perpendicular impinge, the $f_{inh} < -1$ condition requires $\eta > 5$ (Fratzl et al.,

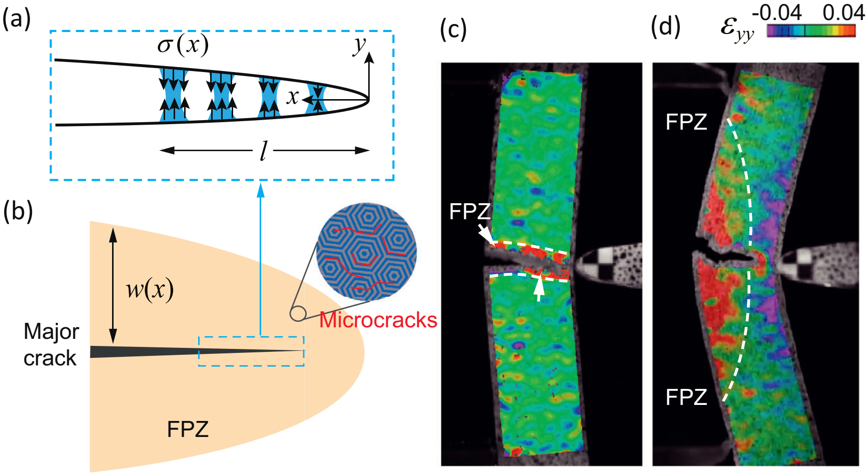

Fig. 14. Toughening mechanisms. (a) and (b) show schematics of the crack bridging and process zone toughening. The toughening effect of microcracking is considered as a fracture process zone (FPZ). (c) and (d) show the normal strain field of a homogeneous beam made of VeroWhite and an architected beam with the concentric hexagonal microstructure. The FPZ marked by dashed lines refers to regions with high residue strain. Scale bars: 1 cm.

2007). The constituents in our experiments give $\eta \approx 100$, thereby, the crack shielding condition is satisfied. This is the theoretical basis why cracks are slowed down by the soft layer (Fig. 12c and Supporting Videos). On the other hand, this crack shielding mechanism can also be explained by the stress concentration factor at the crack tip, which is significantly reduced by the existence of the soft layer with a sufficient thickness (Ji and Gao, 2004).

Crack deflection is another toughening mechanism that prevents catastrophic damage when a crack propagates from a compliant region (E_s) towards a stiff region (E_h). The criteria for judging whether a crack (perpendicular to the interface) will deflect or penetrate the interface depends on the following rule (Ming-Yuan and Hutchinson, 1989)

$$\begin{cases} G_{IF}/G_C < G_d/G_p\ , & \text{deflect} \\ G_{IF}/G_C > G_d/G_p\ , & \text{penetrate} \end{cases} \tag{8}$$

where G_d/G_p is the ratio of driving force between crack deflection and penetration, depending on the parameter $\alpha = (E_h - E_s)/(E_h + E_s)$. G_{IF} and G_C are the fracture toughness of the interface and the material in front of the crack. Assume a crack propagates from Tango Plus towards VeroWhite, $\alpha \approx 1$, giving $G_d/G_p \to \infty$ (Ming-Yuan and Hutchinson, 1989), which means that a crack will always deflect at the interface. On the contrary, when the crack is propagating from the harder layer towards the softer layer, $\alpha \approx -1$, giving $G_d/G_p = 0.5$, which lays the constraint on the crack deflection as $G_{IF}/G_C < 0.5$. The above discussion are accurate for cracks impinging on an interface. The three-point bending condition is a slightly different situation, which can be treated as a propagating crack with an extra tensile stress field due to bending. As a result, cracks propagating from the soft layer toward the hard layer is stopped until the bending load increased to a higher level which itself breaks the hard phase behind the soft layer. Such a process repeats to form the bead-like cracks shown in Fig. 9h, largely suppressing catastrophic damage. The crack deflection theory can also be used to analyze the hybrid beams. For example, the hybrid beam design 1 (Fig. 12a) may be viewed as three-layers with E_1: E_2: $E_3 = 0.344{:}0.256{:}1.08$, corresponding to $G_d/G_p = 0.25$ at the 1-2 interface and $G_d/G_p = 0.5$ at the 2-3 interface. The requirement for crack penetration by Eq. (8) is $G_{IF}/G_C > 0.25$ and $G_{IF}/G_C > 0.5$ at the 1-2 and 2-3 interface respectively. These conditions are satisfied since our 3D printer guarantees a good interface property ($G_{IF}/G_C \sim 1$). This analysis is consistent with the observation that cracks directly penetrates all three layers in hybrid design 1 (Fig. 12a).

Furthermore, the uncracked ligaments behind the crack tip (Fig. 9h-j) can exist over a large distance (l), which limits the crack opening. The effect of bridging on the stress intensity factor at the crack tip can be calculated with (Shang and Ritchie, 1989)

$$K_{tip} = K_a - K_s, \tag{9}$$

$$K_s = \frac{\sqrt{2}}{\pi} \int_0^l \frac{f\sigma(x)}{\sqrt{x}} dx, \tag{10}$$

where K_a and K_s are the driving stress intensity factor and the bridging shield stress intensity factor, respectively. $\sigma(x)$ is the stress in the uncracked ligaments, f is the area fraction occupied by the ligaments over the bridging zone l (Fig. 14a). Formulas for evaluating $\sigma(x)$ in fiber reinforced and staggered microstructures can be found in (Shang and Ritchie, 1989) and (Barthelat and Rabiei, 2011), respectively. Typically, $\sigma(x) \propto \sqrt{E\sigma_y}$, where E and σ_y are the stiffness and yield stress of the ligament. Because Tango Plus has small E and σ_y (compared to VeroWhite), therefore the shielding effect (K_s) is insignificant,

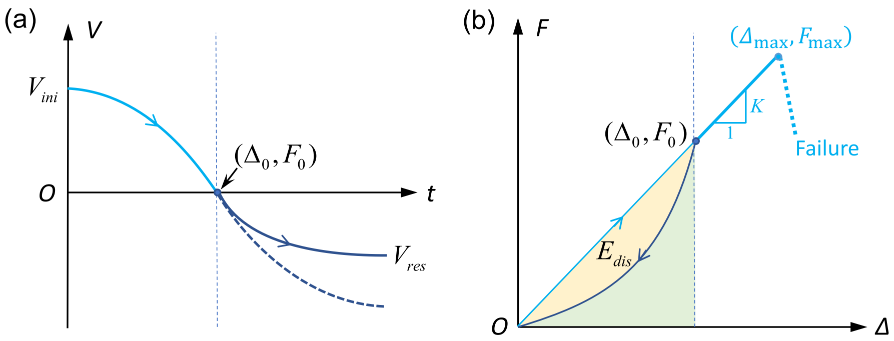

Fig. 15. Modelling the relation between response time and flexibility. (a) Velocity history during an impact event (before damage takes place), the loading and unloading process are marked by light blue and dark blue color respectively. The dashed line indicates no dissipation. (b) Corresponding force-displacement curve. The arrows represent the loading-unloading process before damage (corresponding to the velocity history in (a)). The yellow region represents the amount of energy dissipated. The thick line indicates the failure of a specimen at $\Delta_{\max}$ and $F_{\max}$. (For interpretation of the references to color in this figure legend, the reader is referred to the web version of this article.)

similar to the results reported in nacre ($K_s/K_a\sim$ 0.2% (Barthelat and Rabiei, 2011)) and SiC reinforced composites ($K_s/K_a\sim$ 5% (Shang and Ritchie, 1989)). Although the direct shielding effect of crack bridging is small, it plays an important role in enlarging the crack processing zone and preventing fragmentation. Note that all the proposed architected beams show no fragmentation, and bridging helps the broken beam to stay in one piece (Fig. 12b).

In addition, crack bridging, crack deflection, and crack shielding mechanisms facilitate micro-damages to take place in a larger region. The process zone toughening model provides one approach to evaluate the distributed microcracking effect (Fig. 14b), where the extra toughness introduced in the process zone, ΔJ_P, is formulated as (Evans et al., 1986)

$$\Delta J_P = 2\int_0^w U(y)dy, \tag{11}$$

$$U(y) = \int_0^{\varepsilon(y)} \sigma d\varepsilon, \tag{12}$$

where w is the half width of the process zone, $U(y)$is the energy dissipated per unit area, which depends on the distribution of residual strains $\varepsilon(y)$ and stress σ within the fracture process zone (FPZ). The strain field can be visualized with DIC, Fig. 13c and d shows a comparison of the FPZ size between VeroWhite and the concentric hexagon microstructure, which reveal that the latter one has an FPZ with ~10 times greater size. This is a strong evidence that FPZ plays an important role in the toughening of architected beams (Menig et al., 2000, 2001). In addition, the dissipated energy $U(y)$ may also be stored in the form of shear strain, one example is the layered beam shown in Fig. 9.

Finally, mechanisms such as crack branching and crack twisting also contribute to the toughening of certain material architectures by enforcing mode-mixity and amplifying the surface area per unit crack propagation, which is especially effective when combined with a multiple crack initiation mechanism (Kessler et al., 1996). More discussion may be found in the references (Faber and Evans, 1983; Ravi-Chandar and Knauss, 1984; Suksangpanya et al., 2017), and we have submitted an article with more detailed studies of the fracture of architected materials (Jia and Wang, 2019). It should be noted that while the existing fracture models give useful insights on the high toughness observed in architected beams, these models cannot directly predict the detailed cracking process and the critical condition of crack initialization. Under certain scenarios (e.g., different sample aspect ratios, stiffness ratios and strength ratios of the hard to the soft phase), damage patterns different from the current experimental observations could take place. Examples include wrinkling/kinking in the layer microstructure (Jia et al., 2018b; Pan et al., 2019; Zhang and Latour Jr, 1994) and crack penetrating into the center of the concentric hexagonal microstructure. More studies on the damage patterns of biomimetic composites can be found in (Jia and Wang, 2019).

4.3. Fast response

Simplified velocity history and force-displacement relation of a beam under impact (before damage) is plotted in Fig. 15. Focusing on the detaching process (after the maximum displacement), the velocity can be approximated by a power law $V(t) = -V_{res}t^n/t_R^n$, where t_R is the response time. The corresponding acceleration and displacement are derived as $a(t) = -nV_{res}t^{n-1}/t_R^n$ and $\Delta(t) = V_{res}t^{n+1}/(n+1)t_R^n$. Based on the these equations, force is related to displacement by $F \propto \Delta^{(n-1)/(n+1)}$ and the maximum displacement Δ_0 is related to response time t_R by $\Delta_0 = \Delta(t_R) = V_{res}t_R/(n+1)$, or equivalently,

$$t_R = (n+1)\Delta_0/V_{res}. \tag{13}$$

The incident kinetic energy is stored as the strain energy of the beam. Assuming a linear loading process, $mV_{ini}^2/2 = K\Delta_0^2/2$, so $\Delta_0 = \sqrt{m/K} \cdot V_{ini}$. The definition of dissipation ratio (η) gives $mV_{res}^2/2 = (1-\eta)mV_{ini}^2/2$. Combine with Eq. (13) we derive

$$t_R = (n+1)\sqrt{\frac{\rho \cdot Vol}{K(1-\eta)}}, \tag{14}$$

where *Vol* is the volume of the beam. For a specific beam shape, *Vol* is a constant, and in our specimens the change of effective density ρ is small. Thereby, $t_R \propto (n+1)/\sqrt{K(1-\eta)}$, demonstrating that response time is inversely related to the flexural stiffness K, which is the basis for the stiffness – response rate tradeoff. Moreover, dissipation and n also contribute to the response rate. At $\eta \to 1$, the response time is dominated by the dissipation ratio, while away from this point fast response can be controlled by K. As a conclusion, a moderate to low dissipation ratio is essential for designing a flexible and fast response beam.

Flexibility is defined as a material's ability of deformation without breaking. So, besides low flexural stiffness, another aspect of flexibility is the ability to accommodate large deformations without failure. For simplified analysis, $K \propto F_{\max}/\Delta_{\max}$, Eq. (14) becomes

$$t_R \propto (n+1)\sqrt{\frac{\rho \cdot Vol \cdot \Delta_{\max}}{F_{\max}(1-\eta)}}. \tag{15}$$

Eq. (15) suggests that simultaneously small t_R (fast response) and large $\Delta_{\max}$ (large deformation) can be achieved with a large $F_{\max}$ and a small η, which means high strength and small dissipation. This analysis explains why the concentric hexagonal material (which is relatively strong and have moderate dissipation) shows fast response with good flexibility.

4.3. Future work

While our study provides useful information in the design and selection of material architecture, there are many open questions for further study. First, the size and number of unit cells in the specimen is limited by our 3D printer, which can at most fabricate specimens with three levels of hierarchy. Therefore, new manufacturing methods that can span more length scales and more time efficient are highly desired. Second, the number of unit cells of the concentric hexagon specimen is insufficient in a material homogeneous point of view. Specimens that have more unit cells typically have higher fracture toughness. This is considered as size effect, which is another important topic, where reference (Bažant, 2004; Bazant and Chen, 1997) may be referred to for further study. Third, we've shown that in the hierarchical designs, using different second-order microstructures lead to significant different effective material performances. So, the next question is how to effectively and optimally combine various microstructures into a hierarchical material at different length scales. Fourth, a preferred damage pattern could significantly improve the material's toughness. For this reason, a customized damage model of each microstructure that can predict the criteria of damage pattern transformation and consider the dynamic effect should be developed. Finally, Ashby plots containing all the state of art bulk engineering materials are now available and proven to be useful in bulk material selection (Ashby, 2016). Similarly, we should build an Ashby plot that includes as many material architectures as possible, which will benefit the study of material architectures and facilitate their application.

5. Conclusions

Learning from nature, we've investigated three aspects of biomimetic architected materials: 1) characterizing the dynamic performance of five different bio-mimicking microstructures, including the layer, brick-and-mortar, concentric hexagonal, cross-lamellar, and rotating plywood microstructure; 2) hierarchical design, how to substitute a microstructure with higher order microstructures spanning multiple length scales; and 3) hybrid design – the assembly of different microstructures at a certain length scale.

First, the dynamic performance of each material architecture is characterized by low-velocity three-point bending tests. We show that the layered microstructure is flexible and tough by transferring the tensile/compressive deformations into shear deformations, which exhibits remarkable reusability. The concentric hexagon (isotropic) and brick and mortar (anisotropic) microstructures show a better balance between energy dissipation, response rate, stiffness, strength, and toughness, explaining their ubiquitousness in nature. The cross-lamellar and rotating plywood are stiff but less tough compared to the layer and brick and mortar microstructures. Importantly, the high crack arresting ability of the rotating plywood structure is highly correlated with the specimen's structural shape and requires proper design to maximize its performance. In addition, material indices are adopted to evaluate the overall performance of architected materials which makes material architecture selection straightforward.

Second, while previous theories show that either stiffness and strength, or toughness and strength are exclusive in self-similar hierarchical designs, we demonstrate that using higher order microstructures different from the first order is possible (and necessary) to improve stiffness, strength, and toughness simultaneously. Further, the optimal integration of different microstructures at different hierarchical levels is an interesting topic for further research.

Third, hybrid beams are designed with bio-mimicking and functional gradient approaches. Aside from further improved flexibility, strength, and toughness, hybrid architecture designs provide more control over the deformation field, crack initiation location, and crack propagation pattern. Therefore, they provide promising potential in personal protection armor and shock wave absorber designs, where catastrophic damage and fragmentation should be avoided. Importantly, the hybrid design approach provides an alternative to the hierarchical design approach in improving mechanical performance, which can be more readily manufactured.

Furthermore, we show that material architecture designs can effectively expand the material property space. Importantly, it makes material property combination like strength and toughness, stiffness and dissipation, flexible and fast response possible. The key mechanisms contributed the architecture toughening are 1) crack stopped at the soft layers and 2) enlarged fracture process zone, which is mainly contributed by distributed micro-damages and facilitated by crack deflection, bridging, and branching. These results on the relation between material architecture and material property will potentially facilitate the study and application of architected materials.

Competing interest

The authors declare no competing financial interests.

Acknowledgment

The authors gratefully acknowledge the support from the National Science Foundation (CMMI-1462270) and the Office of Naval Research. Zian Jia thanks Dr. Yanyu Chen (University of Louisville) for helpful discussions. Yang Yu thanks the sponsorship from China Scholarship Council.

Supplementary materials

Supplementary material associated with this article can be found, in the online version, at doi:10.1016/j.jmps.2018.12.015.

References

Aizenberg, J., Weaver, J.C., Thanawala, M.S., Sundar, V.C., Morse, D.E., Fratzl, P., 2005. Skeleton of Euplectella sp.: structural hierarchy from the nanoscale to the macroscale. Science 309, 275–278.

Al-Ketan, O., Assad, M.A., Al-Rub, R.K.A., 2017. Mechanical properties of periodic interpenetrating phase composites with novel architected microstructures. Compos. Struct. 176, 9–19.

Ashby, M.F., 2016. Materials Selection in Mechanical Design. Elsevier Science & Technology Books.

Ashby, M.F., Johnson, K., 2013. Materials and design: the art and science of material selection in product design. Butterworth-Heinemann.

Barthelat, F., Rabiei, R., 2011. Toughness amplification in natural composites. J. Mech. Phys. Solids. 59, 829–840.

Barthelat, F., Tang, H., Zavattieri, P., Li, C.-M., Espinosa, H., 2007. On the mechanics of mother-of-pearl: a key feature in the material hierarchical structure. J. Mech. Phys. Solids. 55, 306–337.

Bažant, Z.P., 2004. Scaling theory for quasibrittle structural failure. Proc. Natl. Acad. Sci. U.S.A. 101, 13400–13407.

Bazant, Z.P., Chen, E.-P., 1997. Scaling of structural failure. Appl. Mech. Rev. 50, 593–627.

Bechthold, M., Weaver, J.C., 2017. Materials science and architecture. Nat. Rev. Mater. 2, 17082.

Berger, J., Wadley, H., McMeeking, R., 2017. Mechanical metamaterials at the theoretical limit of isotropic elastic stiffness. Nature 543, 533–537.

Bertoldi, K., Vitelli, V., Christensen, J., van Hecke, M., 2017. Flexible mechanical metamaterials. Nat. Rev. Mater. 2, 17066.

Bigi, A., Burghammer, M., Falconi, R., Koch, M.H., Panzavolta, S., Riekel, C., 2001. Twisted plywood pattern of collagen fibrils in teleost scales: an X-ray diffraction investigation. J. Struct. Biol. 136, 137–143.

Bouville, F., Maire, E., Meille, S., Van de Moortèle, B., Stevenson, A.J., Deville, S., 2014. Strong, tough and stiff bioinspired ceramics from brittle constituents. Nat. Mater. 13, 508–514.

Bruet, B.J., Song, J., Boyce, M.C., Ortiz, C., 2008. Materials design principles of ancient fish armour. Nat. Mater. 7, 748.

Chen, Y., Jia, Z., Wang, L., 2016. Hierarchical honeycomb lattice metamaterials with improved thermal resistance and mechanical properties. Compos. Struct. 152, 395–402.

Chen, Y., Wang, L., 2016. Harnessing structural hierarchy to design stiff and lightweight phononic crystals. Extreme Mech. Lett. 9, 91–96.

Clegg, W., Kendall, K., Alford, N.M., Button, T., Birchall, J., 1990. A simple way to make tough ceramics. Nature 347, 455–457.

Compton, B.G., Lewis, J.A., 2014. 3D-printing of lightweight cellular composites. Adv. Mater. 26, 5930–5935.

Coulais, C., Sounas, D., Alù, A., 2017. Static non-reciprocity in mechanical metamaterials. Nature 542, 461–464.

Currey, J., Kohn, A., 1976. Fracture in the crossed-lamellar structure ofConus shells. J. Mater. Sci. 11, 1615–1623.

Currey, J.D., 1999. The design of mineralised hard tissues for their mechanical functions. J. Exp. Biol. 202, 3285–3294.

Devadas, M., 2003. Reinforced concrete design. Tata McGraw-Hill Education.

Dimas, L.S., Bratzel, G.H., Eylon, I., Buehler, M.J., 2013. Tough composites inspired by mineralized natural materials: computation, 3D printing, and testing. Adv. Funct. Mater. 23, 4629–4638.

Evans, A.G., Ahmad, Z., Gilbert, D., Beaumont, P., 1986. Mechanisms of toughening in rubber toughened polymers. Acta Metall 34, 79–87.

Faber, K.T., Evans, A.G., 1983. Crack deflection processes—I. Theory. Acta metallurgica 31, 565–576.

Fratzl, P., 2007. Biomimetic materials research: what can we really learn from nature's structural materials? J. Royal Soc. Interface 4, 637–642.

Fratzl, P., Gupta, H.S., Fischer, F.D., Kolednik, O., 2007. Hindered crack propagation in materials with periodically varying Young's modulus—lessons from biological materials. Adv. Mater. 19, 2657–2661.

Gao, H., 2006. Application of fracture mechanics concepts to hierarchical biomechanics of bone and bone-like materials. Int. J. Fract. 138, 101.

Gorishnyy, T., Maldovan, M., Ullal, C., Thomas, E., 2005. Sound ideas. Phys. World 18, 24.

Gu, G.X., Libonati, F., Wettermark, S.D., Buehler, M.J., 2017a. Printing nature: Unraveling the role of nacre's mineral bridges. J. Mech. Behav Biomed. Mater. 76, 135–144.

Gu, G.X., Takaffoli, M., Buehler, M.J., 2017b. Hierarchically Enhanced Impact Resistance of Bioinspired Composites. Adv. Mater. 29, 1700060.

Jackson, A., Vincent, J., Turner, R., 1988. The mechanical design of nacre. Proc. R. Soc. Lond., B, Biol. Sci. 234, 415–440.

Ji, B., Gao, H., 2004. A study of fracture mechanisms in biological nano-composites via the virtual internal bond model. Mater. Sci. Eng. A 366, 96–103.

Jia, Z., Chen, Y., Yang, H., Wang, L., 2018a. Designing Phononic Crystals with Wide and Robust Band Gaps. Phys. Rev. Appl. 9, 044021.

Jia, Z., Li, T., Chiang, F.-p., Wang, L., 2018b. An experimental investigation of the temperature effect on the mechanics of carbon fiber reinforced polymer composites. Compos. Sci. Technol 154, 53–63.

Jia, Z., Wang, L., 2019. 3D printing of biomimetic composites with improved fracture toughness, under review.

Jia, Z., Yu, Y., Wang, L., 2019. Learning from nature: use material architecture to break the performance tradeoffs, under review.

Kadic, M., Bückmann, T., Stenger, N., Thiel, M., Wegener, M., 2012. On the practicability of pentamode mechanical metamaterials. Appl. Phys. Lett. 100, 191901.

Kessler, H., Ballarini, R., Mullen, R.L., Kuhn, L.T., Heuer, A.H., 1996. A biomimetic example of brittle toughening:(I) steady state multiple cracking. Comput. Mater. Sci. 5, 157–166.

Khelif, A., Djafari-Rouhani, B., Vasseur, J., Deymier, P., 2003. Transmission and dispersion relations of perfect and defect-containing waveguide structures in phononic band gap materials. Phys. Rev. B 68, 024302.

Klatt, T., Haberman, M.R., 2013. A nonlinear negative stiffness metamaterial unit cell and small-on-large multiscale material model. J. Appl. Phys. 114, 033503.

Lakes, R., 1993. Materials with structural hierarchy. Nature 361, 511.

Lakes, R., 2009. Viscoelastic materials. Cambridge University Press.

Launey, M.E., Buehler, M.J., Ritchie, R.O., 2010. On the mechanistic origins of toughness in bone. Ann. Rev. Mater. Res. 40, 25–53.

Lawn, B.R., Lee, J.J.-W., Chai, H., 2010. Teeth: among nature's most durable biocomposites. Ann. Rev. Mater. Res 40, 55–75.

Libonati, F., Gu, G.X., Qin, Z., Vergani, L., Buehler, M.J., 2016. Bone inspired materials by design: Toughness amplification observed using 3D printing and testing. Adv. Eng. Mater. 18, 1354–1363.

Liu, L., Ding, Q., Zhong, Y., Zou, J., Wu, J., Chiu, Y.-L., Li, J., Zhang, Z., Yu, Q., Shen, Z., 2018. Dislocation network in additive manufactured steel breaks strength–ductility trade-off. Mater. Today 21, 354–361.

Lu, K., 2016. Stabilizing nanostructures in metals using grain and twin boundary architectures. Nat. Rev. Mater. 1, 16019.

Lu, L., Shen, Y., Chen, X., Qian, L., Lu, K., 2004. Ultrahigh strength and high electrical conductivity in copper. Science 304, 422–426.

Maldovan, M., 2013. Sound and heat revolutions in phononics. Nature 503, 209.

Martin, J.H., Yahata, B.D., Hundley, J.M., Mayer, J.A., Schaedler, T.A., Pollock, T.M., 2017. 3D printing of high-strength aluminium alloys. Nature 549, 365.

Martin, J.J., Fiore, B.E., Erb, R.M., 2015. Designing bioinspired composite reinforcement architectures via 3D magnetic printing. Nat. Commun 6, 8641.

Menig, R., Meyers, M., Meyers, M., Vecchio, K., 2000. Quasi-static and dynamic mechanical response of Haliotis rufescens (abalone) shells. Acta Mater 48, 2383–2398.

Menig, R., Meyers, M., Meyers, M., Vecchio, K., 2001. Quasi-static and dynamic mechanical response of Strombus gigas (conch) shells. Mater. Sci. Eng. A 297, 203–211.

Meyers, M.A., McKittrick, J., Chen, P.-Y., 2013. Structural biological materials: critical mechanics-materials connections. Science 339, 773–779.

Meza, L.R., Zelhofer, A.J., Clarke, N., Mateos, A.J., Kochmann, D.M., Greer, J.R., 2015. Resilient 3D hierarchical architected metamaterials. Proc. Natl. Acad. Sci 112, 11502–11507.

Ming-Yuan, H., Hutchinson, J.W., 1989. Crack deflection at an interface between dissimilar elastic materials. Int. J. Solids Struct. 25, 1053–1067.

Mirkhalaf, M., Dastjerdi, A.K., Barthelat, F., 2014. Overcoming the brittleness of glass through bio-inspiration and micro-architecture. Nat. Commun. 5, 3166.

Montemayor, L., Chernow, V., Greer, J.R., 2015. Materials by design: Using architecture in material design to reach new property spaces. MRS Bull. 40, 1122–1129.

Munch, E., Launey, M.E., Alsem, D.H., Saiz, E., Tomsia, A.P., Ritchie, R.O., 2008. Tough, bio-inspired hybrid materials. Science 322, 1516–1520.

Nicolaou, Z.G., Motter, A.E., 2012. Mechanical metamaterials with negative compressibility transitions. Nat. Mater. 11, 608–613.

Ovid'ko, I., Sheinerman, A., 2015. Toughening due to crack deflection in ceramic-and metal-graphene nanocomposites. Rev. Adv. Mater. Sci. 43, 52–60.

Pan, F., Wang, G., Liu, L., Chen, Y., Zhang, Z., Shi, X., 2019. Bending induced interlayer shearing, rippling and kink buckling of multilayered graphene sheets. J. Mech. Phys. Solids. 122, 340–363.

Raney, J.R., Compton, B.G., Mueller, J., Ober, T.J., Shea, K., Lewis, J.A., 2018. Rotational 3D printing of damage-tolerant composites with programmable mechanics. Proc. Natl. Acad. Sci. 201715157.

Ravi-Chandar, K., Knauss, W., 1984. An experimental investigation into dynamic fracture: III. On steady-state crack propagation and crack branching. Int. J. Fract. 26, 141–154.

Ritchie, R.O., 2011. The conflicts between strength and toughness. Nat. Mater. 10, 817.

Roland, C., 2006. Mechanical behavior of rubber at high strain rates. Rubber Chem. Technol. 79, 429–459.

Schaedler, T.A., Carter, W.B., 2016. Architected cellular materials. Ann. Rev. Mater. Res. 46, 187–210.

Schaedler, T.A., Jacobsen, A.J., Torrents, A., Sorensen, A.E., Lian, J., Greer, J.R., Valdevit, L., Carter, W.B., 2011. Ultralight metallic microlattices. Science 334, 962–965.

Shang, J.K., Ritchie, R., 1989. Crack bridging by uncracked ligaments during fatigue-crack growth in SiC-reinforced aluminum-alloy composites. Metall. Trans. A 20, 897–908.

Shin, Y.A., Yin, S., Li, X., Lee, S., Moon, S., Jeong, J., Kwon, M., Yoo, S.J., Kim, Y.-M., Zhang, T., 2016. Nanotwin-governed toughening mechanism in hierarchically structured biological materials. Nat. Commun. 7, 10772.

Standard, A., 2010. Standard test method for tensile properties of plastics. ASTM International, West Conshohocken, PA.

Studart, A.R., 2012. Towards high performance bioinspired composites. Adv. Mater 24, 5024–5044.

Suksangpanya, N., Yaraghi, N.A., Kisailus, D., Zavattieri, P., 2017. Twisting cracks in Bouligand structures. J. Mech. Behav. Biomed. Mater. 76, 38–57.

Velasco-Hogan, A., Xu, J., Meyers, M.A., 2018. Additive Manufacturing as a Method to Design and Optimize Bioinspired Structures. Adv. Mater. 1800940.

Wang, L., Boyce, M.C., Wen, C.Y., Thomas, E.L., 2009a. Plastic Dissipation Mechanisms in Periodic Microframe-Structured Polymers. Adv. Funct. Mater. 19, 1343–1350.

Wang, L., Lau, J., Thomas, E.L., Boyce, M.C., 2011. Co-continuous composite materials for stiffness, strength, and energy dissipation. Adv. Mater. 23, 1524–1529.

Wang, L.F., Song, J.H., Ortiz, C., Boyce, M.C., 2009b. Anisotropic design of a multilayered biological exoskeleton. J. Mater. Res. 24, 3477–3494.

Wang, Z., Nakamura, T., 2004. Simulations of crack propagation in elastic–plastic graded materials. Mech. Mater. 36, 601–622.

Weaver, J.C., Milliron, G.W., Miserez, A., Evans-Lutterodt, K., Herrera, S., Gallana, I., Mershon, W.J., Swanson, B., Zavattieri, P., DiMasi, E., 2012. The stomatopod dactyl club: a formidable damage-tolerant biological hammer. Science 336, 1275–1280.

Wegst, U.G., Bai, H., Saiz, E., Tomsia, A.P., Ritchie, R.O., 2015. Bioinspired structural materials. Nat. Mater. 14, 23.

Yamamoto, T., Domon, T., Takahashi, S., Islam, N., Suzuki, R., 2000. Twisted plywood structure of an alternating lamellar pattern in cellular cementum of human teeth. Anat. Embryol. 202, 25–30.

Yao, H.M., Dao, M., Imholt, T., Huang, J.M., Wheeler, K., Bonilla, A., Suresh, S., Ortiz, C., 2010. Protection mechanisms of the iron-plated armor of a deep-sea hydrothermal vent gastropod. P. Natl. Acad. Sci. USA 107, 987–992.

Zhang, G., Latour Jr, R.A., 1994. An analytical and numerical study of fiber microbuckling. Compos. Sci. Technol. 51, 95–109.

Zhang, P., Heyne, M.A., To, A.C., 2015. Biomimetic staggered composites with highly enhanced energy dissipation: Modeling, 3D printing, and testing. J. Mech. Phys. Solids. 83, 285–300.

Zhang, Z., Zhang, Y.-W., Gao, H., 2011. On optimal hierarchy of load-bearing biological materials. Proc. R. Soc. Lond., B, Biol. Sci. 278, 519–525.

Zhao, R., Sider, K.L., Simmons, C.A., 2011. Measurement of layer-specific mechanical properties in multilayered biomaterials by micropipette aspiration. Acta Biomaterialia 7, 1220–1227.

Zheng, X., Lee, H., Weisgraber, T.H., Shusteff, M., DeOtte, J., Duoss, E.B., Kuntz, J.D., Biener, M.M., Ge, Q., Jackson, J.A., 2014. Ultralight, ultrastiff mechanical metamaterials. Science 344, 1373–1377.